Van Allen probes, NOAA, GOES, and ground observations of an intense EMIC wave event extending over 12 h in magnetic local time

M. J. Engebretson[1], J. L. Posch[1], J. R. Wygant[2], C. A. Kletzing[3], M. R. Lessard[4], C.-L. Huang[4], H. E. Spence[4], C. W. Smith[4], H. J. Singer[5], Y. Omura[6], R. B. Horne[7], G. D. Reeves[8], D. N. Baker[9], M. Gkioulidou[10], K. Oksavik[11,12], I. R. Mann[13,14], T. Raita[15], and K. Shiokawa[16]

[1]Department of Physics, Augsburg College, Minneapolis, Minnesota, USA, [2]School of Physics and Astronomy, University of Minnesota, Twin Cities, Minneapolis, Minnesota, USA, [3]Department of Physics and Astronomy, University of Iowa, Iowa City, Iowa, USA, [4]Space Science Center, University of New Hampshire, Durham, New Hampshire, USA, [5]Space Weather Prediction Center, NOAA, Boulder, Colorado, USA, [6]Research Institute for Sustainable Humanosphere, Kyoto University, Kyoto, Japan, [7]British Antarctic Survey, Cambridge, UK, [8]Space Science and Applications Group, Los Alamos National Laboratory, Los Alamos, New Mexico, USA, [9]Laboratory for Atmospheric and Space Physics, University of Colorado Boulder, Boulder, CO, USA, [10]The Johns Hopkins University Applied Physics Laboratory, Laurel, Maryland, USA, [11]Birkeland Centre for Space Science, Department of Physics and Technology, University of Bergen, Bergen, Norway, [12]The University Centre in Svalbard, Longyearbyen, Norway, [13]Department of Physics, University of Alberta, Edmonton, Alberta, Canada, [14]NASA/Goddard Space Flight Center, Greenbelt, Maryland, USA, [15]Sodankylä Geophysical Observatory, University of Oulu, Sodankylä, Finland, [16]STELAB, Nagoya University, Toyokawa, Japan

Abstract Although most studies of the effects of electromagnetic ion cyclotron (EMIC) waves on Earth's outer radiation belt have focused on events in the afternoon sector in the outer plasmasphere or plume region, strong magnetospheric compressions provide an additional stimulus for EMIC wave generation across a large range of local times and L shells. We present here observations of the effects of a wave event on 23 February 2014 that extended over 8 h in UT and over 12 h in local time, stimulated by a gradual 4 h rise and subsequent sharp increases in solar wind pressure. Large-amplitude linearly polarized hydrogen band EMIC waves (up to 25 nT p-p) appeared for over 4 h at both Van Allen Probes, from late morning through local noon, when these spacecraft were outside the plasmapause, with densities ~5–20 cm^{-3}. Waves were also observed by ground-based induction magnetometers in Antarctica (near dawn), Finland (near local noon), Russia (in the afternoon), and in Canada (from dusk to midnight). Ten passes of NOAA-POES and METOP satellites near the northern foot point of the Van Allen Probes observed 30–80 keV subauroral proton precipitation, often over extended L shell ranges; other passes identified a narrow L shell region of precipitation over Canada. Observations of relativistic electrons by the Van Allen Probes showed that the fluxes of more field-aligned and more energetic radiation belt electrons were reduced in response to both the emission over Canada and the more spatially extended emission associated with the compression, confirming the effectiveness of EMIC-induced loss processes for this event.

1. Introduction

The focus of this paper is on the widespread electromagnetic ion cyclotron (EMIC) waves observed by the twin Van Allen Probes spacecraft (originally denoted Radiation Belt Storm Probes, RBSP), by proton detectors on the low-altitude NOAA and METOP satellites, and by ground-based magnetometer arrays in Finland, Antarctica, Canada, and Russia during a strong solar wind compression on 23 February 2014, and on losses of ultrarelativistic electrons in Earth's outer radiation belt associated with these waves. Previous studies of the impact of solar wind compressions have produced mixed results: *Millan and Thorne* [2007] suggested that radiation belt electron losses due to solar wind compressions could be a result of electron precipitation, whereas observations using low-altitude polar-orbiting POES satellites by *Horne et al.* [2009] found little evidence of precipitation associated with these types of events. The comprehensive ground- and space-based observations reported here provide a new set of data that can help assess the importance of compression-induced precipitation from a different perspective.

Cornwall [1965] and *Liemohn* [1967] were some of the first to describe how temperature anisotropies in hot electrons and protons were unstable, via cyclotron instabilities, to the generation of VLF and ULF waves,

respectively. While generation of these waves clearly came at the expense of their respective unstable particle populations and tended to cause reductions in their fluxes because of the induced pitch angle diffusion that led to subsequent increased precipitation into the ionosphere, depletion of relativistic radiation belt electrons by EMIC waves was also suggested in early theoretical studies over three decades ago [*Thorne and Kennel*, 1971; *Lyons and Thorne*, 1972] and more recently included as one of several major loss processes by *Horne and Thorne* [1998] and *Millan and Thorne* [2007]. During this past decade the effectiveness of EMIC waves has been tested and significantly circumscribed [e.g., *Summers and Thorne*, 2003; *Summers et al.*, 2007a, 2007b; *Shprits et al.*, 2013]. In particular, *Shprits et al.* [2013] pointed out that EMIC-induced scattering should be more effective than other loss processes for electrons with energies above 2 MeV.

Two recent studies have further refined the parameters for effectiveness of these waves in depleting relativistic electrons. *Usanova et al.* [2014] used Van Allen Probes Relativistic Electron Proton Telescope (REPT) data in conjunction with ground-based Canadian Array for Realtime Investigations of Magnetic Activity (CARISMA) observations of EMIC waves to show that the loss of highly relativistic radiation belt electrons (2–8 MeV) caused by EMIC wave interactions was confined to pitch angles below ~45°. *Usanova et al.* [2014] also presented model pitch angle diffusion calculations that were consistent with these observations: diffusion was very fast at low pitch angles and significantly (orders of magnitude) slower toward high pitch angles, and also increased significantly with energy from 2.3 MeV to 7.1 MeV. *Kersten et al.* [2014] performed a simulation study of the effectiveness of EMIC waves in causing losses of electrons from the radiation belts, using EMIC wave data from the CRRES satellite mission and found these waves caused a significant reduction in the electron flux for energies greater than 2 MeV but only for pitch angles lower than about 60°.

Although it is well documented that solar wind compressions stimulate EMIC wave activity in the outer dayside magnetosphere [e.g., *Olson and Lee*, 1983; *Anderson and Hamilton*, 1993; *Fuselier et al.*, 2004], in the past decade a number of event studies and statistical surveys have shown that large increases in solar wind dynamic pressure can stimulate compressions of the magnetosphere across a wide range of local times. *Lee et al.* [2005] presented examples showing significant variation in the nightside response to solar wind dynamic pressure pulses (often a simple magnetic field compression at all local times but in other cases depressions near midnight) and *Lee et al.* [2007] noted that large purely compressional events (with no substorm onset) led to overall global (and quasi-simultaneous in magnetic local time (MLT)) increases of energetic neutral atom fluxes, due to ions adiabatically energized by the compressions.

A statistical study by *Lyons et al.* [2005] found a similar result: under not strongly southward interplanetary magnetic field (IMF) conditions, solar wind dynamic pressure enhancements compressed the entire magnetosphere, leading to a prompt global auroral enhancement (both dayside and nightside) with no evidence for substorm bulge-region aurora or current wedge formation. They pointed out that such global enhancements of the aurora could not be related to an azimuthally localized current wedge and seemed clearly to be a result of the global energization of magnetospheric particles by the compression of the magnetosphere that accompanies an enhancement in dynamic pressure. However, under steady, strongly southward IMF conditions, *Lyons et al.* [2005] found that a dynamic pressure enhancement was found to cause both compressive auroral brightening away from the bulge region and a Harang region substorm auroral brightening. These two auroral enhancements merged together, leading to a very broad auroral enhancement covering ~10–15 h of MLT.

Although the above studies did not specifically look at EMIC waves or the proton aurora they can stimulate, other more recent studies have done so. *Meurant et al.* [2003] traced the progression of both proton and electron aurora in MLT and UT toward the nightside after a strong solar wind compression on 28 April 2001 following an extended interval of very quiet solar wind and IMF conditions. Nightside proton precipitation was stimulated at slightly lower latitude than the electron aurora, and the location of proton precipitation on the nightside was distributed symmetrically across the midnight–noon axis.

Zhang et al. [2005] studied a number of nightside detached auroras (NDA) during highly disturbed conditions using auroral imager data from Thermosphere Ionosphere Mesosphere Energetics and Dynamics (TIMED) spacecraft and Imager for Magnetopause-to-Aurora Global Exploration (IMAGE) spacecraft as well as DMSP particle data, and found that NDA occurred during the recovery phase of intense magnetic storms

Table 1. Coordinates of GOES 13 and 15

Station	SM Latitude	UT of Local Noon	L
GOES 13	10°N	17:12	6.8
GOES 15	4.5°N	21:21	6.6

($Dst < -130$) or a growth phase with sudden increase of Dst, and were located between 1900 and 0300 MLT. *Zhang et al.* [2008] described an event on 21 January 2005 when a fast interplanetary shock compressed the magnetosphere and caused detached proton auroras in the dayside, duskside, and nightside ionosphere. EMIC waves were directly associated with the dayside subauroral emissions, and ring current simulations suggested that ~10 keV protons were the source of the duskside and nightside subauroral emissions. *Søraas et al.* [2013] reported two instances of nightside postmidnight subauroral proton precipitation at ring current energies and proton auroras observed during the recovery phases of a two-main-phase storm; in each case the intensity and longitudinal extension of the arc were modulated by the solar wind dynamic pressure.

In contrast to the localized dusk sector EMIC waves stimulated by fresh injections of ring current ions often used in simulations during the main phase of a magnetic storm, the compression-related waves reported here occurred prior to the onset of a magnetic storm (the third in 4 days) and were accompanied by little evident substorm activity. Because of the large amplitude of these waves and their unusually large extent in local time and L shell this event provides a clear demonstration of the effectiveness of EMIC waves stimulated by strong solar wind compressions in depleting radiation belt electrons. In section 2 below we describe the instrumentation used in this study. Section 3 describes the geomagnetic conditions during this event and presents wave observations from the Van Allen Probes, from other high-altitude spacecraft, and from ground-based magnetometer arrays. Section 4 presents NOAA/METOP observations of precipitating ring current protons. Section 5 presents Van Allen Probes observations of ultrarelativistic electrons during and after this intense wave event, and section 6 provides a discussion and summary of these observations, of several recent theoretical studies of the effects of EMIC waves on these electrons, and of their implications.

2. Data Sources

The Van Allen Probes consist of two identically instrumented spacecraft with apogees of 5.8 R_E, perigee ~ 600 km, and an orbital period of 9 h. Their near-equatorial orbits are inclined 10° with respect to the equator, enabling nominal sampling to magnetic latitudes of $0° \pm 21°$ [*Mauk et al.*, 2013]. Magnetometer data used in this study were obtained by the EMFISIS (Electric and Magnetic Field Instrument Suite and Integrated Science) instrument package, which measures vector magnetic fields at a cadence of 64 vector samples/s, for a Nyquist rate of 32 Hz [*Kletzing et al.*, 2013].

The Electric Fields and Waves (EFW) instrument on the Van Allen Probes uses two orthogonal centripetally deployed booms in the spin plane with tip-to-tip separations of 100 m to measure vector electric fields in the spin plane at a cadence of 32 vector samples/s, for a Nyquist rate of 16 Hz [*Wygant et al.*, 2013]. The third component of the electric field is measured by two spherical sensors separated by ~15 m, deployed at the ends of two stacer booms oppositely directed along the spin axis of the spacecraft. In addition, the potential of the orthogonal booms was used to determine the plasma number density.

Energetic ions and electrons were measured using several instruments. As part of the Energetic Particle, Composition, and Thermal Plasma (ECT) suite [*Spence et al.*, 2013] relativistic electron fluxes were measured by the Relativistic Electron Proton Telescope (REPT) [*Baker et al.*, 2013], which points perpendicular to the spin axis of the spacecraft. REPT resolves electrons with energies from ~1.6 MeV to ~20 MeV. Ions with energies from ≤ 20 eV or spacecraft potential (whichever is greater) to ≥ 45 keV were measured by the ECT/HOPE (Helium Oxygen Proton Electron) mass spectrometer instrument [*Funsten et al.*, 2013].

Geomagnetic field conditions at geostationary orbit (6.6 R_E) were determined using vector fluxgate magnetometer data from the GOES 13 and 15 spacecraft [*Singer et al.*, 1996]. Table 1 lists the coordinates of these spacecraft. Data were sampled at a 0.512 s cadence, for a Nyquist frequency of 0.976 Hz.

EMIC waves were observed during this interval of solar wind compression by four ground arrays of induction (search coil) magnetometers: (1) Halley (L = 4.7) and South Pole Station (L = 14.1) [*Engebretson et al.*, 2008a]

Table 2. Coordinates of the Search Coil Magnetometer Sites Used in This Study[a]

Station	Geographic		Geomagnetic		L	UT of Local Noon
	Latitude	East Longitude	Latitude	East Longitude		
Halley	−75.50	333.40	−62.26	29.89	4.69	1444
Ivalo	68.55	27.28	65.37	107.87	5.85	0908
Ministik Lake	53.35	247.03	60.47	309.26	4.18	2001
Magadan	60.0	150.9	54.25	220.69	2.98	0237
Mondy	51.62	100.92	47.41	174.78	2.22	0519

[a]Corrected geomagnetic coordinates and universal time (UT) of local magnetic noon (MLT) have been computed for epoch 2014 and an altitude of 100 km using the NSSDC Modelweb facility (http://omniweb.gsfc.nasa.gov/vitmo/cgm_vitmo.html).

and AAL-PIP PG4 (L = 9.7) [*Musko et al.,* 2009] in Antarctica; (2) Kilpisjarvi (L = 5.9—partial data), Ivalo (L = 5.8), Sodankyla (L = 5.2), Rovaniemi (L = 4.9—partial data), and Nurmijarvi (L = 3.3), part of the Finnish pulsation magnetometer chain [*Yahnina et al.,* 2008]; (3) Fort Churchill (L = 7.23), Dawson (L = 6.12), Ministik Lake (L = 4.18), Rabbit Lake (L = 6.44), and Thief River Falls (L = 3.53), part of the CARISMA induction coil array [*Mann et al.,* 2008]; and (4) Magadan, Russia (L = 2.97) and Moshiri, Japan (L = 1.63), part of the Solar-Terrestrial Environment Laboratory (STEL) induction magnetometer network [*Shiokawa et al.,* 2010]. No higher-latitude station in the STEL array recorded useful data on this day. Shown here are data from Halley, Ivalo, Ministik Lake, and Magadan, representative of the other stations in their respective arrays, and with the largest wave amplitudes. We also show induction magnetometer data from Mondy, Siberia, part of the United Geomagnetic Observatory of the Solar-Terrestrial Physics Institute, Irkutsk, Russia. Table 2 lists the geographic and geomagnetic coordinates for these five stations, along with their L shells and the universal time of local noon.

EMIC waves, with frequencies in the Pc1 and Pc2 range (with frequencies between 0.1 and 5.0 Hz) have traditionally been observed using magnetometers, both on the ground and in space. Because a necessary consequence of ion cyclotron wave emission is scattering of hot protons into the loss cone, during the past decade low Earth orbit observations of localized, subauroral precipitation of ring current protons by the NOAA POES and METOP spacecraft, in Sun-synchronous near-polar orbits at ~ 850 km altitude, have been shown to be a useful proxy for the occurrence of EMIC waves in the same regions [e.g., *Sakaguchi et al.,* 2007; *Sandanger et al.,* 2007; *Yahnin et al.,* 2009; *Usanova et al.,* 2010]. In this study we also use POES and METOP observations, in particular from the Medium Energy Proton and Electron Detector (MEPED) [*Evans and Greer,* 2000], which detects ions in three energy bands (30–80, 80–250, and 250–800 keV) but provides neither mass resolution nor charge state. One detector at each energy looks upward along the Earth-satellite radial vector and views ions in the local loss cone, while the other MEPED detector looks normal to the first detector and observes ions slightly outside the loss cone.

3. Observations

Figure 1 presents the solar wind and interplanetary magnetic field (IMF) context within which this wave event occurred. As the data shown in Figure 1 indicates, near 0200 UT on 20 February the solar wind velocity V_{sw} increased rapidly to over 700 km/s (Figure 1d) and the IMF north-south B_z component began the first of two negative excursions to near −10 nT (Figure 1c), resulting in a magnetic storm with a double main phase (with minima of the *SYM-H* index of −102 nT at 0555 UT and −95 nT at 1145 UT, Figure 1h). After an initial rapid recovery later that day, a gradual increase of *SYM-H* for several days was interrupted only by small decreases near the beginning and end of 22 February. Following a solar wind proton density and flow pressure increase (Figures 1e and 1f) during 23 February, the IMF B_z component again turned southward (Figure 1c), prompting another, weaker magnetic storm (with *SYM-H* minimum of − 63 nT at 2250 UT). No subsequent geomagnetic activity occurred until late on 27 February.

Figure 2 shows a more detailed view of the context of this event, from 0100 to 1100 UT on 23 February. The IMF exhibited mostly gradual variations from being mostly sunward (B_x largest, Figure 2a) from 0100 to 0300 UT, mostly northward (B_z largest, Figure 2c) from 0330 to 0700 UT, sunward and eastward from 0700 to 0800 UT, and mostly westward from 0800 to 1000 UT, at which time B_z became more southward.
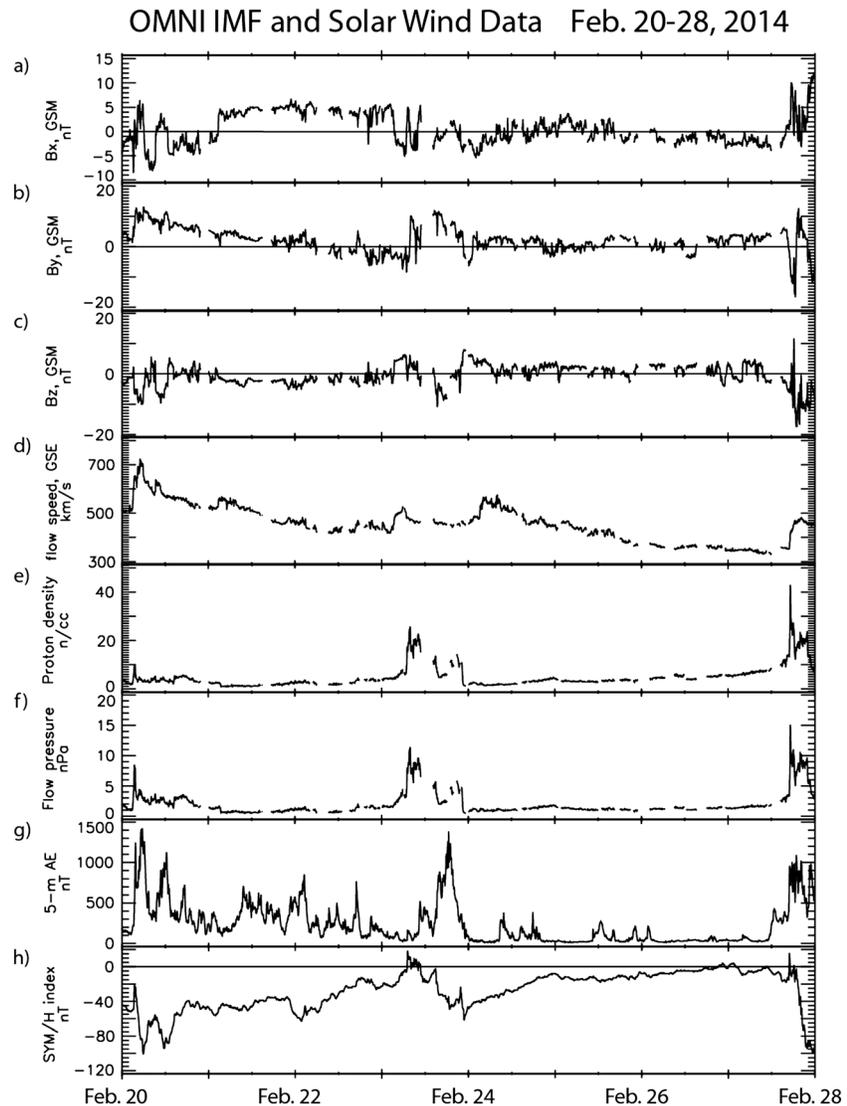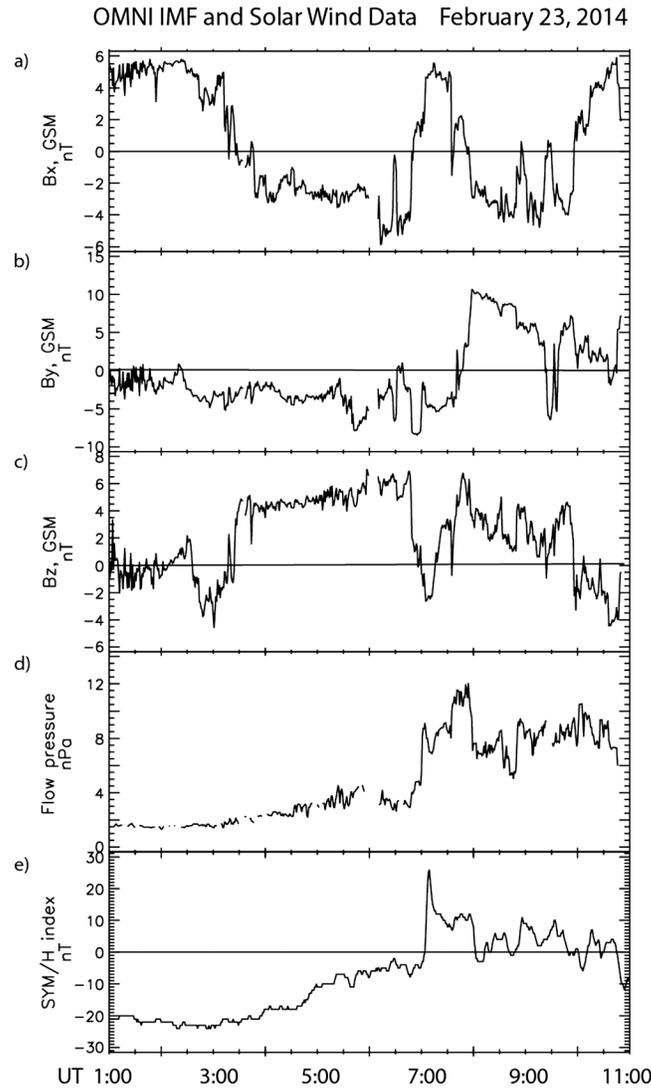
Figure 1. Five minute averaged solar wind and interplanetary magnetic field (IMF) data timeshifted to the nose of the bow shock, obtained from the OMNI database at http://cdaweb.gsfc.nasa.gov from 00 UT 20 February to 00 UT 28 February 2014. (a–c) The *x*, *y*, and *z* components of the IMF in GSM coordinates. (d) The solar wind flow speed, (e) the solar wind plasma density, (f) the solar wind pressure, (g) the 5 min *AE* index, and (h) the *SYM-H* index.

The solar wind flow pressure (P_{sw}, Figure 2d) was steady from 0100 to 0300 UT, increased gradually from 0300 to 0600 UT, and after a slight decrease rose sharply to 8.5 nPa at 0700 UT. P_{sw} rose further during the next hour and dropped sharply at 0800 UT, but continued at levels above 6 nPa until 1100 UT. The *SYM-H* index (Figure 2e) tracked the gradual increase and sharp rise of P_{sw}, from 0100 to 0700, and remained above or near 0 nT throughout the interval. The good correlation between low-latitude magnetic records (on which the *Dst* and *SYM-H* indices are based) and solar wind pressure variations during northward IMF conditions has been well documented [e.g., *Francia et al.,* 1999, and references therein], and qualitatively corresponds to increases in the Chapman-Ferraro currents at the magnetopause.

3.1. Van Allen Probes Wave Observations

Figure 3 shows observations from three instruments on RBSP-B: a 0–5 Hz Fourier spectrogram of differenced EMFISIS magnetic field data (Figure 3a), the local electron density determined from the spacecraft potential recorded by the EFW spin plane booms (Figure 3b), and the spin-averaged differential proton flux measured by the HOPE instrument (Figure 3c). The magnetic local time (MLT), magnetic latitude (MLAT), and spacecraft

Figure 2. One minute averaged solar wind and interplanetary magnetic field (IMF) data timeshifted to the nose of the bow shock, obtained from the OMNI database at http://cdaweb.gsfc.nasa.gov from 01 UT to 11 UT 23 February 2014. (a–c) The x, y, and z components of the IMF in GSM coordinates. (d) The solar wind flow pressure, and (e) the *SYM-H* index, respectively.

altitude data (R_E, in Earth radii) shown below Figure 3b were obtained from the Satellite Situation Center (SSCweb) facility at NASA/Goddard Space Flight Center. The MacIlwain L shell parameter was calculated for 90° pitch angle electrons using the OP77Q [*Olson and Pfitzer*, 1982] external magnetic field model and the International Geomagnetic Reference Field (IGRF) internal magnetic field model, and the Roederer L* parameter [*Roederer*, 1970] was calculated for 90° pitch angle electrons using the TS05 [*Tsyganenko and Sitnov*, 2005] external field model and the IGRF internal magnetic field model.

Shown in Figure 3a is the B_y (east-west) transverse component of the differenced magnetic field, in local field-aligned coordinates. Differencing is used in these Fourier spectrograms to facilitate display of a wide range of spectral power by removing the f^{-2} falloff in spectral power with frequency, while retaining information about the absolute background intensity. *Anderson et al.* [1992a] and *Takahashi et al.* [1990] give a quantitative relationship between spectral power calculated from differenced and undifferenced data. EMIC waves between 2 and 2.5 Hz appeared near 0240 UT (0900 MLT), immediately after the spacecraft passed outward through a sharp plasmapause (Figure 3b), and approximately at the time P_{sw} began its gradual increase (Figure 2d). There was no evidence of a plasmaspheric plume during the times waves were observed; the electron density varied gradually with L throughout the apo-

gee pass, and waves appeared only during times the electron density n_e was below 20 cm^{-3}. All the wave power from 0220 through 0800 UT (near 1400 MLT) was near or above the yellow line in Figure 3a, which shows the local He$^+$ gyrofrequency (Ω_{He+}), thus in the "hydrogen band." During the first part of the wave interval these waves were at or near Ω_{He+}. After 0700 UT, however, these waves often filled a substantial fraction of the band from Ω_{He+} to Ω_{H+}. Because RBSP-B was located south of the magnetic equator (from ~ −20° to −14° MLAT during the wave interval), we infer that the waves were most likely generated closer to the magnetic equator, where the magnitude of B on these field lines was slightly lower. An intense but still sinusoidal burst of wave activity appeared between 0705 and 0707 UT, coincident with a sudden 34 nT increase and overshoot in the total magnetic field (evident in the white Ω_{H+} line in Figure 3a). Intense wave activity resumed after 0717 but ceased at 0758 UT (near 1350 MLT) well before the spacecraft reentered the plasmasphere at or after 0835 UT.
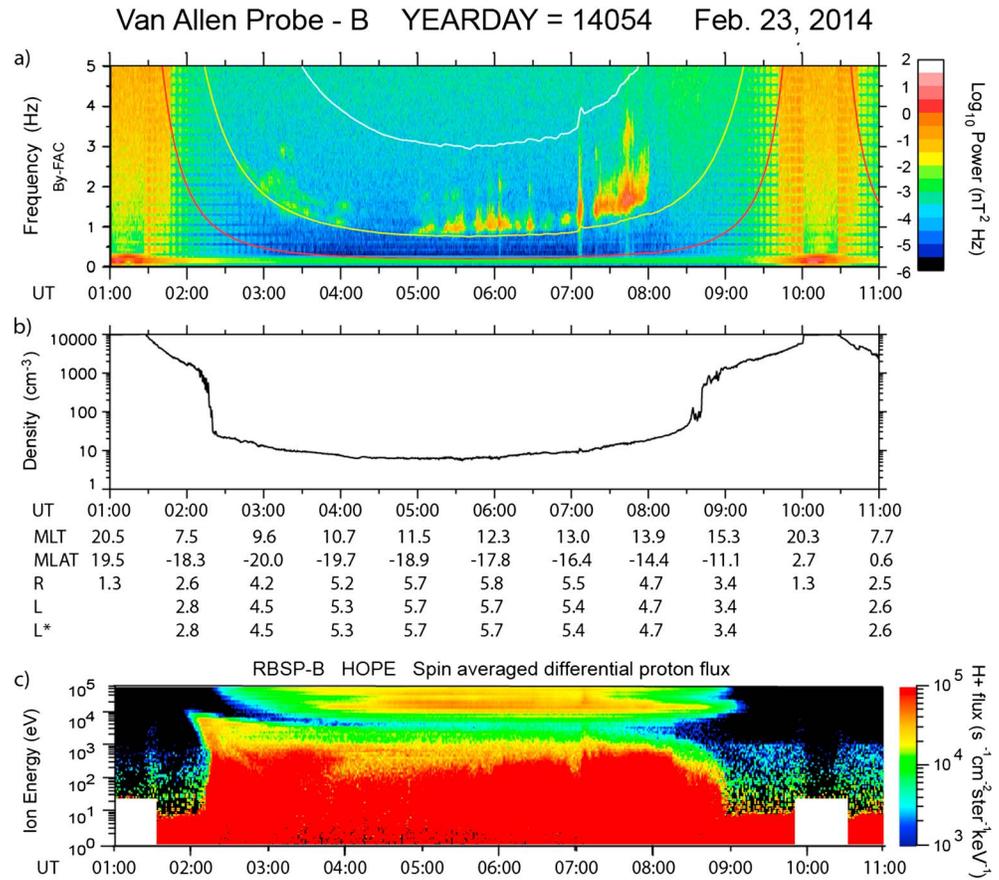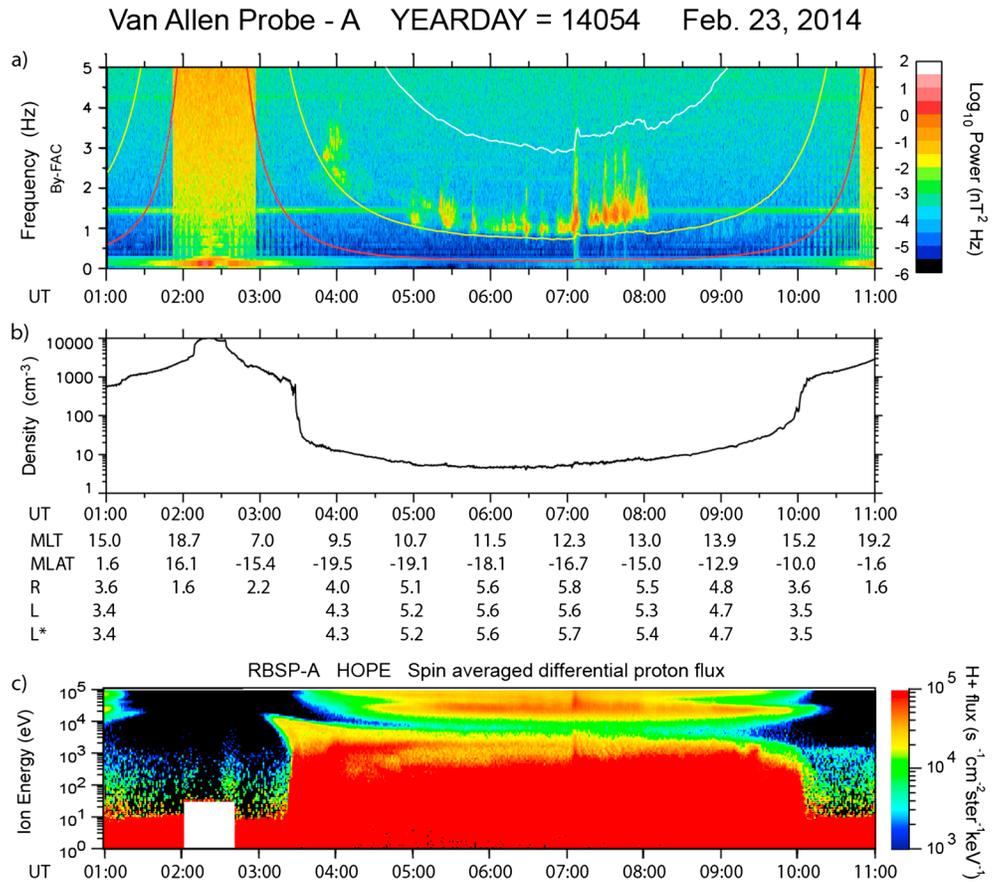
Figure 3. Stacked plot of RBSP-B EMFISIS, EFW, and HOPE data from 01 to 11 UT 23 February 2014. (a) The B_y (east-west) transverse component of the magnetic field in local field-aligned coordinates. The vertical axis in this panel shows frequency from 0 to 5 Hz and power in nT^2-Hz is encoded according to the color bar at the right. Total magnetic field data were used to calculate the local H^+, He^+, and O^+ gyrofrequencies, which are plotted in white, yellow, and red, respectively. (b) The electron density determined from the spacecraft potential recorded by the EFW spin plane booms. (c) The spin-averaged differential proton flux measured by the HOPE instrument.

EMIC waves appeared essentially continuously (but with considerable variation in amplitude) in the L shell range from 4 to 5.7 (apogee). HOPE proton data (Figure 3c) showed enhanced ring current fluxes with energy centered near 10 keV during the entire duration of the wave event, beginning near the time RBSP-B exited the plasmasphere and decreasing gradually at and after the time it reentered the plasmasphere. Large fluxes of plasma sheet protons (<1 keV) were also present during the entire wave event.

RBSP-A, in a similar orbit but ~ 1 h behind RBSP-B, first observed strong Pc1 waves near 0340 UT (0900 MLT), when it also passed outside the plasmapause (Figure 4). The frequency of these waves was also above Ω_{He^+}. The spurious constant tone at 1.4 Hz was produced by a heater near the sensor. A similarly intense sinusoidal wave burst appeared between 0705 and 0707 coincident with a 35 nT increase in B, and intense waves ceased near 0758 UT (1300 MLT), but much less intense waves in the helium band appeared between 0840 and 0950 UT. HOPE proton data (Figure 4c) again showed enhanced ring current and plasma sheet fluxes during the duration of the wave event.

The end of intense waves at both RBSP spacecraft at 0758 UT occurred simultaneous with a rapid decrease in total magnetic field. The 15 nT decrease at RBSP-A can be seen in both the white and the yellow traces in Figure 4a, but the significantly smaller decrease at RBSP-B (−4 nT) is not easily discernible in the yellow trace in Figure 3a.

Wave amplitudes at both RBSP spacecraft often exceeded 5 nT and at 0705 UT peaked above 12 nT (RBSP-A) and 10 nT (RBSP-B); amplitudes also peaked at 11 nT (B) at 0741 and 0743 UT. These amplitudes are

Figure 4. Stacked plot of RBSP-A EMFISIS, EFW, and HOPE data from 01 to 11 UT 23 February 2014, as in Figure 3.

sufficiently large for nonlinear effects to occur: Figure 5 shows a 0 to 5 Hz Fourier spectrogram from 0700 to 0800 UT of the transverse components of RBSP-A magnetic field data (a and b) in local field-aligned coordinates, as well as their color-coded ellipticity (c), where −1 indicates left-hand circular polarization, 0 indicates linear polarization, and +1 indicates right-hand circular polarization. Rising-tone-triggered emissions [*Pickett et al.*, 2010; *Omura et al.*, 2010; *Grison et al.*, 2013] with both linear and left-hand polarizations were observed (at both spacecraft) when the waves were most intense, for example, at RBSP-A between 0726 and 0729 UT. With the exception of these rising tones, the waves were predominantly linearly polarized. This is consistent with the GOES 10 observations of hydrogen band waves and simulated spectra presented by *Denton et al.* [2014] and with the statistical results of *Anderson et al.* [1992b].

3.2. Wave Observations at Geosynchronous Orbit and on the Ground

Figure 6 shows 0–1 Hz Fourier spectrograms of differenced HE component (radially inward) magnetic field data from (a) GOES 13 and (b) GOES 15 and of differenced X component (north-south) search coil (dB/dT) data from (c) Halley, Antarctica, (d) Ivalo, Finland, (e) Mondy, Russia, (f) Magadan, Russia, and (g) Ministik Lake, Canada, from 0100 to 1100 UT 23 February 2014. Figure 6a also shows the local He$^+$ and O$^+$ gyrofrequencies as white overplotted lines, and Figure 6b shows these frequencies as well as the H$^+$ gyrofrequency during the last 4 h of the time interval shown. Figure 6h repeats the OMNI flow pressure from Figure 2e.

No sustained EMIC wave activity appeared at GOES 13 during the interval shown. The 0708 UT solar wind pressure spike was associated with decreases in total B field at both GOES 13 and 15 (Figures 6a and 6b). No waves were observed during this time at GOES 13 (L = 6.8, 0204 MLT), but at GOES 15 (L = 6.6, 2200 MLT) there was a nearly simultaneous 0.2–0.5 Hz wave burst with amplitude up to 3 nT, followed by <1 nT amplitude activity near 0.2 Hz for ~30 min. The onset of EMIC wave activity at GOES 15 associated
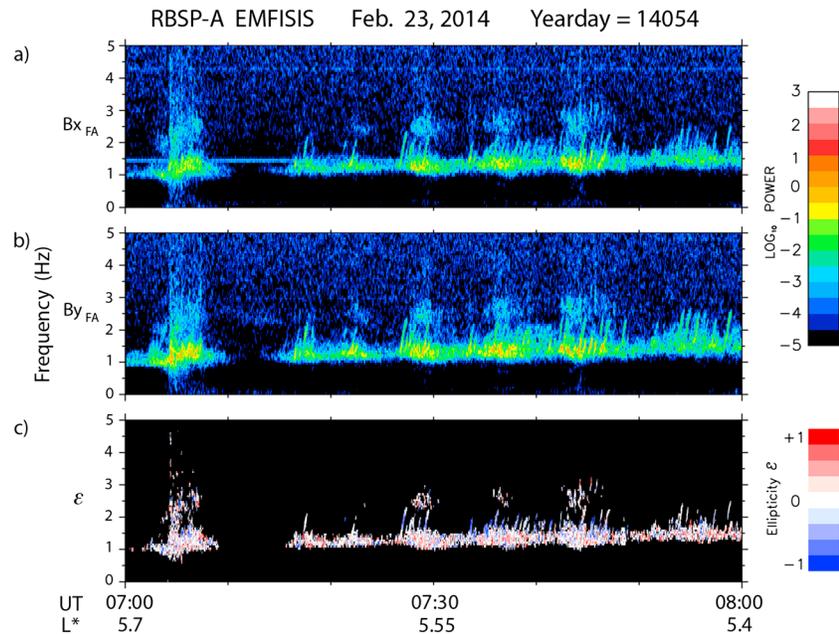
Figure 5. Spectrograms of the transverse components of RBSP-A EMFISIS magnetic field data and their ellipticity from 0700 to 0800 UT 23 February 2014. (a) The B_x (radial) component and (b) the B_y (east-west) transverse component of the magnetic field in local field-aligned coordinates. The vertical axis in these panels shows frequency from 0 to 5 Hz, and power in nT^2-Hz is encoded according to the color bar at the right of these panels. (c) The ellipticity, with blue indicating left-hand polarization and red indicating right-hand polarization according to the color bar at the right. The ellipticity is blanked out if the wave power level is less than 10^{-3} nT^2-Hz in both the B_x and the B_y components.

with a local reduction in total magnetic field (as opposed to an increase) is an example of the variability in nightside responses to solar wind dynamic pressure pulses reviewed in section 1. The 0800 UT solar wind pressure drop was accompanied by a small increase in B at GOES 13 (L = 6.8, 0255 MLT), and a strong ~0.5 Hz wave burst. The total field at GOES 15 continued to drop from 0710 to ~0915 UT and exhibited a slight decrease at 0800 UT (L = 6.6, 2251 MLT); beginning at 0740, the GOES 15 magnetometer data were dominated by broadband noise.

The solar wind pressure spike at 0708 UT caused wave bursts to appear at all five ground stations, and compression-related wave activity appeared between ~0710 and 0800 UT at all ground stations except Ministik Lake, which was then located near midnight local time. At Halley (Figure 6c) wave activity near 2 Hz began weakly at 0220 UT (23.7 MLT), intensified slightly at 0240 UT (0 MLT), at the same time it appeared at RBSP-B (at ~9 MLT), and fell gradually in frequency to ~1 Hz near 0400 UT. Wave power from 0.5 to ~3 Hz (probably ducted from a range of L shells, as will be discussed below) appeared from 5 to 7 UT, as Halley moved from 2.2 to 4.2 MLT. An intense wave burst with continuous frequency from 0.5 to 3.5 Hz appeared at 0708, shortly after the large jump in solar wind pressure. Moderately strong, relatively wideband wave power resumed at Halley from 0715 to 0800 UT, and bursts of medium to strong wave power between 0.7 and 1.7 Hz continued from 0820 to 1050 UT, as it rotated into the postdawn local time sector (~8 MLT).

Wave activity at Ivalo (Figure 6d) began with the burst at 0708 UT, and from that time to 1050 UT closely resembled that observed at Halley, despite their 6 h difference in MLT. This activity also resembled that observed at RBSP-A from 0700 until 0950 UT, when that spacecraft moved into the plasmasphere, except that wave power at Ivalo remained similar both before and after 0800 UT, but power decreased greatly at RBSP-A after 0800 UT.

Wave activity at Mondy (Figure 6e) began weakly near 0540 UT (~1225 MLT), near the time of a strong wave burst at RBSP-B, and was most intense from 0708 to 0800 UT (1350–1440 MLT), during the time of the strongest magnetospheric compression. Weaker wave power appeared between 0830 and 1040 UT, with temporal variations very similar to those observed at Halley and Ivalo, each separated by several hours in local time.

February 23, 2014   YEARDAY 14054
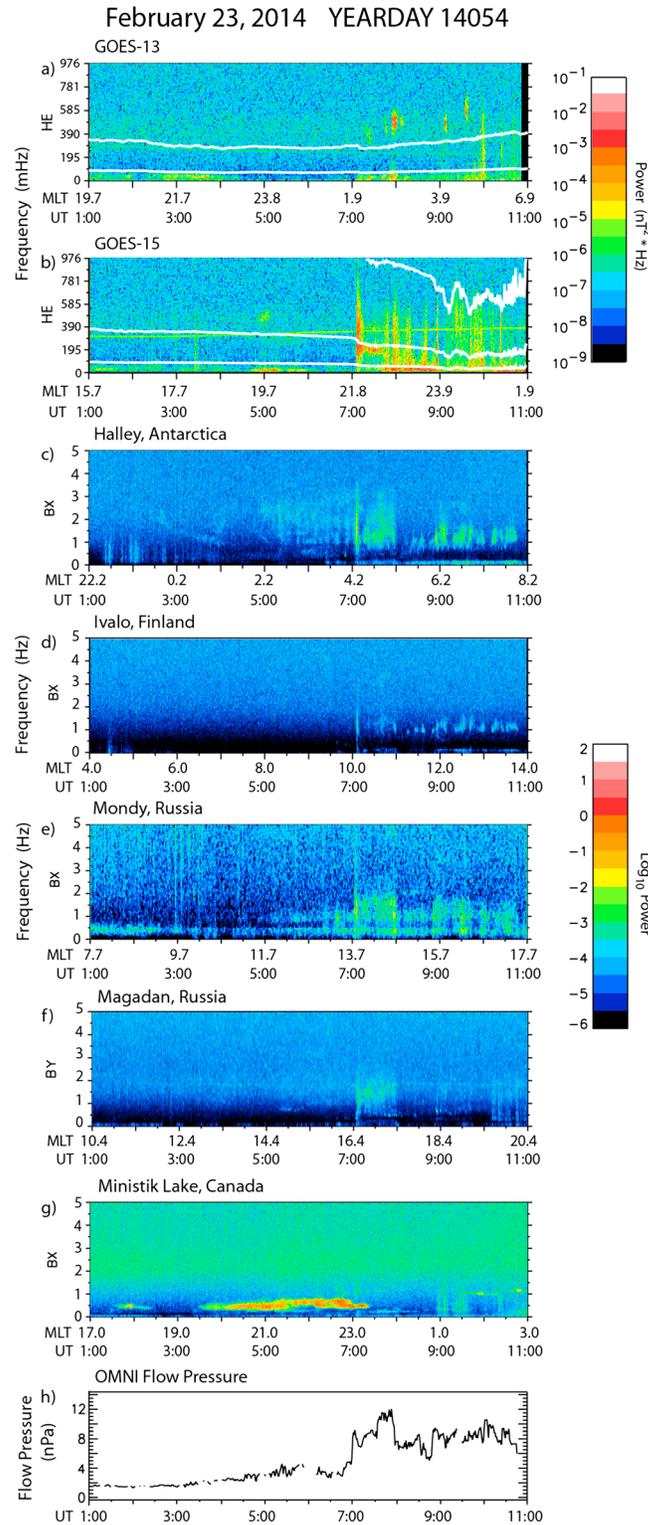
Wave activity at Magadan (Figure 6f), located in the late afternoon sector, appeared above background levels from 0708 UT to 0800 UT (1630–1720 MLT). During this interval the wave occurrence and intensity matched that seen at Mondy (in the early afternoon sector) and at Halley (in the predawn sector) quite well. Weaker wave activity appeared at Magadan near 0900 and from ~1015 to 1040 UT, again with some similarities to the activity observed at Halley, Ivalo, and Mondy.

Wave activity at Ministik Lake (Figure 6g, representative of that observed at several CARISMA stations) was observed from 0130 to 0230 UT near dusk, and more intense continuous activity was observed from 0330 to 0730 UT, near midnight local time. Wave frequencies remained between 0.2 and 0.8 Hz throughout this interval, and, except for the weak burst at 0708 UT, the wave activity showed no similarity to the waves observed at the GOES, RBSP, or Time History of Events and Macroscale Interactions during Substorms (THEMIS) spacecraft. This lack of similarity, as well as the relatively low frequency, suggests that these waves may have been generated by westward drifting freshly injected ring current ions. Two short-lived increases in the *AE* index near the end of the previous day (to 771 nT at 1655 UT and to 340 nT at 2105 UT, Figure 1)

Figure 6. Fourier spectrograms of differenced HE component fluxgate magnetometer data from (a) GOES 13 and (b) GOES 15, and of differenced north-south (*x*) component search coil (d*B*/d*T*) data from (c) Halley, Antarctica, (d) Ivalo, Finland, (e) Mondy, Russia, (f) Magadan, Russia, and (g) Ministik Lake, Canada, from 0100 to 1100 UT 23 February 2014. The vertical axis in Figures 6a and 6b shows frequency from 0 to 0.976 Hz, and power in nT^2-Hz is encoded according to the color bar at the right. Total magnetic field data were used to calculate the local H$^+$, He$^+$, and O$^+$ gyrofrequencies, which are overplotted in white and described in the text. The vertical axis in Figures 6c–6g shows frequency from 0 to 5 Hz, and power in arbitrary units is encoded according to the color bar at the right. Figure 6h repeats Figure 2d showing the solar wind flow pressure.
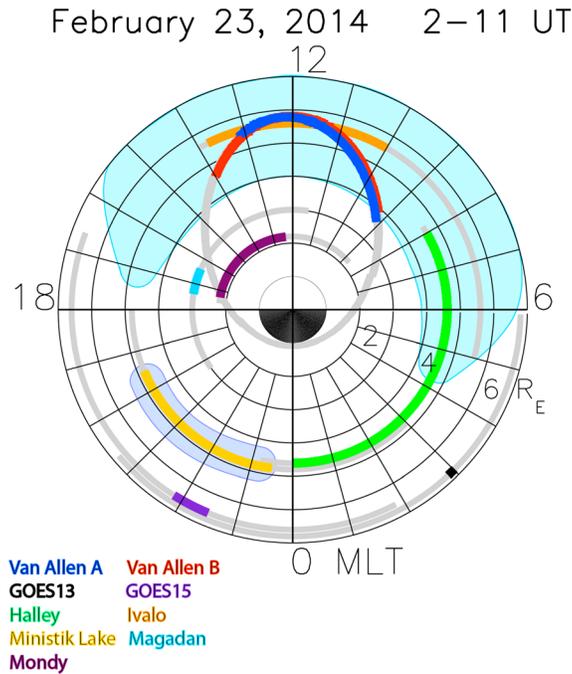
Figure 7. A plot of the L versus MLT locations of five ground stations (Halley, Antarctica; Ivalo, Finland; Mondy, Russia; Magadan, Russia; and Ministik Lake, Canada) and four spacecraft (Van Allen Probes A and B and GOES 13 and 15) that observed EMIC waves during the 23 February 2014 compression event. Narrow gray curves indicate locations as a function of time from 0200 to 1100 UT (time increases counterclockwise), and wider curves indicate locations at which EMIC waves were observed. POES data were used to specify the L shell for the Ministik Lake curve, as explained in the text. Shown in light blue is an inferred demarcation of the region within which hydrogen band waves were observed between 0700 and 0800 UT. The region in which helium band waves were observed is shown in light purple.

may indicate injections of ring current protons that could occasion the observed dusk sector waves, but the *AE* index was very low from 0000 to 1000 UT on 23 February.

Figure 7 is a schematic summary of the locations at and inside geosynchronous orbit where EMIC waves were detected between 0100 and 1100 UT on this day. Narrow-colored curves in this figure show the locations in MLT and L shell of Van Allen Probes A and B, of GOES 13 and 15, and of Halley, Ivalo, Mondy, Magadan, and Ministik Lake. Because of latitudinal ducting in the ionosphere, the L shell of the observing ground station may not match the L shell on which the EMIC wave occurred. In the case of Ministik Lake, however, POES overflights observed localized proton precipitation at $L = 4.8$ (as detailed in the next section), and this value was used in Figure 7.

The light blue shaded region in the upper part of Figure 7 is an inferred demarcation of the region within which hydrogen band waves were observed between 0700 and 0800 UT. We have limited the L shell range, using the lower L limits of waves observed by RBSP-A and -B, to $L \sim 4$. The upper L limit was set to $L = 6$, based on POES/METOP observations of subauroral proton precipitation that often reached to even higher magnetic latitudes. The local time range extends from predawn (4.2 MLT, based on Halley data, Figure 6c) to near dusk (17.4 MLT, based on Magadan data, Figure 6f).

The approximate region in which helium band waves were observed in the dusk sector is shown in light purple, extending slightly in both MLT and L from the orange line in Figure 7 that depicts the MLT extent of activity at Ministik Lake.

To the best of our knowledge, no other high-altitude spacecraft observed significant EMIC wave activity in the inner magnetosphere during this time interval. THEMIS A, D, and E all observed short bursts of EMIC waves, but all except an interval of weak 0.7 Hz waves near 0550 UT at 1520 MLT, $L \sim 6.2$ occurred beyond $L = 6.6$. The Cluster spacecraft were in the solar wind upstream of the bow shock, $\sim 10\,R_E$ south of the Sun-Earth line, and GEOTAIL was $\sim 30\,R_E$ upstream from Earth, $\sim 10\,R_E$ north of the Sun-Earth line.

4. NOAA/METOP Observations

Observations of precipitating protons by the MEPED instrument on NOAA and METOP spacecraft serve two purposes in this study. First, observations in the dusk sector provide information on the L shells at which the EMIC activity detected by CARISMA magnetometers originated. Second, observations in the late morning and noon sector confirm the presence of EMIC activity over a range of L shells, thus extending the single-point observations of the RBSP spacecraft.

Table 3. Times and Locations of NOAA/METOP Observations of Precipitating Protons in the 30–80 and 80–250 keV Energy Ranges in the Dusk Sector

Spacecraft	Time (UT)	Hemisphere	Magnetic Local Time	L Shell Range
NOAA 16	0349	North	20.3	4.69–4.92
NOAA 15	0354	South	19.8	4.48–4.63
METOP 02	0413	North	20.4	4.69–5.02

Three passes in the dusk sector near 0400 UT observed narrow latitudinal bands of precipitating protons in the 30–80 keV and 80–250 keV channels at subauroral latitudes (Table 3). Figure 8 shows data from the NOAA 16 spacecraft, which observed a narrow spike of 30–250 keV precipitating protons between 62.5 and 63.2° MLAT (highlighted with gray shading), with fluxes essentially equal to those of trapped protons, while the >30 keV electrons were still mostly trapped. The narrow proton spike was located well equatorward of the auroral zone, which is the wider area of high proton flux between 67 and 72° MLAT in Figure 8. Two other spacecraft (NOAA 15 and METOP 02) traversed the same magnetic local time region a few minutes later and observed similarly intense, narrow spikes (data not shown). Based on these observations, we used a value of L = 4.8 to plot the MLT location of the CARISMA observations of EMIC waves shown in Figure 8.

Ten Northern Hemisphere passes of NOAA and METOP spacecraft near the magnetic foot point of the RBSP/Van Allen Probes provide proxy information on the L shell extent of the EMIC wave region between 0430 and 0930 UT. A detailed presentation of two of these passes is given in Appendix A, and Figure 9 shows a stacked plot of the 30–80 keV channel from all 10 passes. In this figure time runs downward and is indicated in each panel as the time of closest conjunction between NOAA/METOP and RBSP-A and -B. Black arrows are used to highlight intense spikes of subauroral proton precipitation. Gray shading shows the approximate magnetic latitude of RBSP-A and -B, indicating that during several passes the lowest-latitude precipitation appeared at the same MLAT traversed by the Van Allen Probes. Consistent with Figures 3 and 4, no subauroral energetic proton precipitation was observed before 0500 or after 0800 UT. In addition, consistent with the wider range of frequencies of enhanced EMIC wave power seen in the Halley data than in the Ministik Lake data, and the observations by RBSP-A and -B of strong EMIC wave power from L ~ 4 out to their apog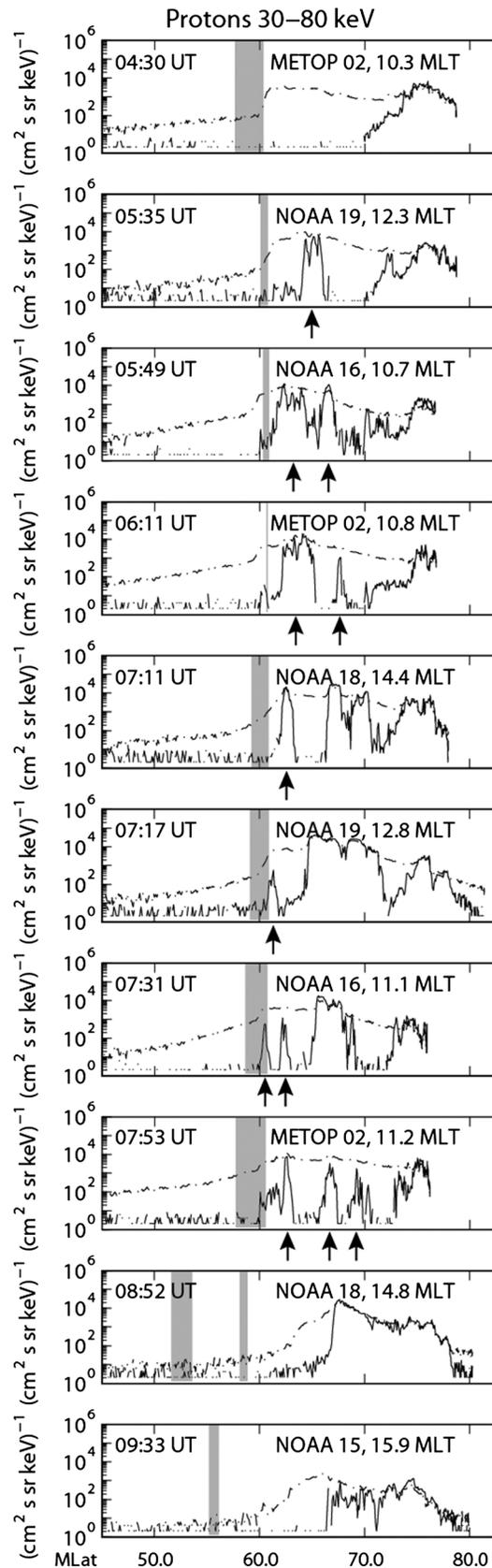ees beyond L = 6, this succession of passes shows spikes of subauroral proton precipitation over a wide temporally varying range of magnetic latitudes, from ~60 to over 65° and at times 70° MLAT, as indicated by the black arrows in Figure 9. The latitudinal width of the proton spikes varied from ~1° to over 3°. On several passes up to three subauroral proton spikes are evident (e.g., METOP 02 at 0753 UT and possibly NOAA 18 at 0711 UT).
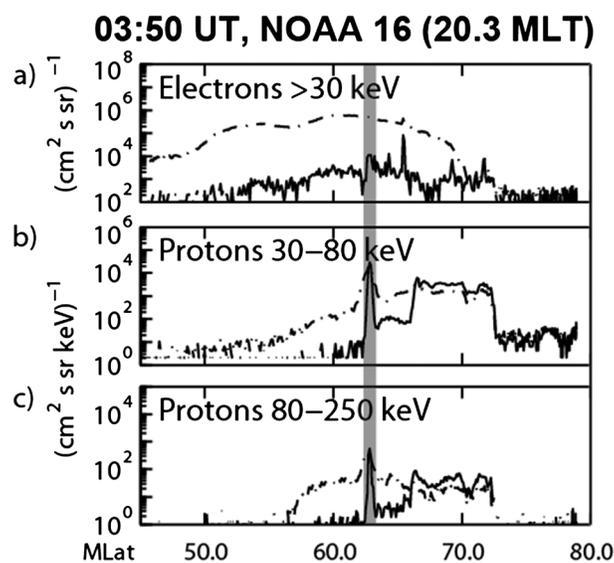
Figure 8. Trapped (dash-dotted lines) and precipitating (solid lines) energetic particle fluxes observed by the MEPED instrument on NOAA 16 during its pass through the dusk local time sector near 0350 UT 23 February 2014. Fluxes of (a) >30 keV electrons, (b) 30–80 keV protons, and (c) 80–250 keV protons, respectively.

5. Effects on Radiation Belt Electrons

Figure 10 shows pitch angle distributions of differential electron fluxes at L* = 4.5 in the 2.3, 4.5, and 5.6 MeV energy channels, respectively, from RBSP-A and -B REPT level 3 data from 20 to 27 February 2014. The colors correspond to the logarithm of the
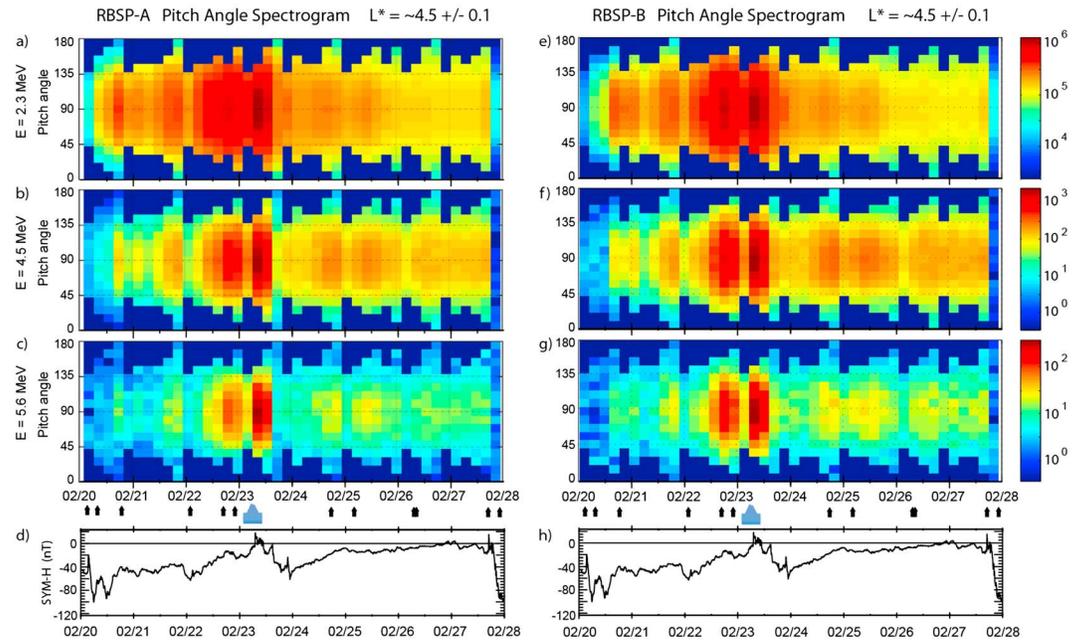
Figure 9. NOAA 30–80 keV precipitating proton data for a series of 10 dayside NOAA/METOP passes between 0430 and 0930 UT on 23 February 2014. Time runs downward, and the approximate time of closest conjunction between NOAA and the Van Allen Probes is indicated in each panel. Gray shading shows the approximate magnetic latitude of RBSP-A and -B, and black arrows highlight intense spikes of subauroral precipitation.

fluxes, in units of $cm^{-2} s^{-1} sr^{-1} MeV^{-1}$. Figures 10d and 10h repeat the *SYM-H* index for these same days from Figure 1h.

Fluxes in all three energy ranges were low at the beginning of 20 February, but by 1200 UT, after the second large rise in *Dst* after a ~100 nT double-peaked storm, they had increased by roughly an order of magnitude. A further flux increase occurred near the end of 21 February, after which time a small storm caused reductions in fluxes, again in all three energy ranges. Larger flux increases, more isotropic in the 2.3 MeV range (Figures 10a and 10e) than in the higher energy ranges (Figures 10b, 10c, 10f, and 10g), occurred near the end of 22 February. A subsequent drop in flux, clearest in the two higher energy ranges, occurred at both spacecraft during the second pass on 23 February. This was followed immediately by the largest flux increase of this interval, beginning near the time of the large solar wind compression on 23 February. Fluxes in all three energy ranges decreased after ~1800 UT 23 February, with steeper drops occurring at the higher energies, during the main phase of a −60 nT storm. Fluxes in all three energy ranges also decreased during half orbits near the beginning of 25 and 26 February and decreased sharply during the main phase of a ~100 nT storm at the end of 27 February.

The black arrows above Figures 10d and 10h indicate the times of intervals of strong EMIC waves observed by either of the Van Allen Probes outside L = 3 (Table 4), and the blue arrow indicates the duration of strong EMIC waves on 23 February 2014. No strong EMIC waves were observed at Halley or at stations in the Finnish, CARISMA, or STEL arrays except those already noted on 23 February, but we note that the available ground stations covered only a limited range of local times. We note also that during the 20–28 February interval, even though RBSP-A and -B were separated by only 1 h along very similar trajectories, only two instances of strong near-simultaneous wave activity at both spacecraft occurred, the first during the long compression-induced wave interval on 23 February,

Figure 10. Pitch angle spectra of relativistic electron fluxes observed by the REPT instrument on (a–c) RBSP-A and (e–g) RBSP-B from 20 to 27 February 2014. Figures 10a–10c and 10e–10g show pitch angle distributions of differential electron fluxes at $L* = 4.5 \pm 0.1$ in the 2.3, 4.5, and 5.6 MeV energy channels, respectively. The colors correspond to the logarithm of the fluxes, in units of $cm^{-2} s^{-1} sr^{-1} MeV^{-1}$, according to the color bars at the right of each panel. Figures 10d and 10h repeat the *SYM-H* index from Figure 1h for these same days. Black arrows above Figures 10d and 10h indicate intervals of strong EMIC waves observed by either of the Van Allen Probes, and the blue arrow indicates the interval of EMIC waves from 0100 to 0800 UT 23 February 2014.

and the second between 0700 and 0840 on 26 February, during which wave activity at the two spacecraft occurred roughly 1 h earlier at RBSP-B than at RBSP-A. Although during this latter event, the waves occurred at similar MLT and L shell values, they did not overlap (Table 4). All the EMIC events observed by only one of the Van Allen Probes during this interval were thus highly localized in both space and in time.

Figure 11 shows this same REPT flux data as Figure 10, but normalized by the 90° pitch angle flux and using a linear color bar scale, following the format used by *Usanova et al.* [2014]. Note that the relativistic electron flux levels during the period in October 2012 shown by *Usanova et al.* [2014] were an order of magnitude higher

Table 4. Intense EMIC Wave Events Observed by the Van Allen Probes, 20–28 February 2014

| Date	Spacecraft	Time (UT)	Band	Magnetic Local Time	L Shell Range	Frequency
Feb. 20	B	0325–0350	H	10.7–11.0	5.5–5.9	1.4–2.0 Hz
	A	0600–0715	He	11.6–12.4	6.2–6.3	0.2–0.4 Hz
	B	1750–1800	He	15.3–15.7	3.4–3.0	1.0–1.4 Hz
Feb. 22	B	0235	H	12.1	6.3	0.6–1.1 Hz
	B	1800–1830	H	9.9–10.4	4.3–4.8	1.6–2.2 Hz
	B	2030–2140	H	12.0–12.7	5.8–5.6	0.8–1.2 Hz
Feb. 23	A,B	0240–0800	H	9.2–13.8	4.0–6.4	0.9–3.5 Hz
Feb. 24	A	1700–1730	H, He	10.9–11.3	5.2–5.5	0.4–1.2 Hz
Feb. 25	B	0350–0400	He	12.7–12.8	6.1–6.0	0.3–0.4 Hz
Feb. 26	B	0700–0720	He	12.7–12.9	6.0–5.8	0.4–0.5 Hz
	A	0800–0840	He	13.0–13.6	5.8–5.2	0.5–0.6 Hz
Feb. 27	B	1710–1810	H, He	11.93–12.1	5.6–5.8	0.5–1.4 Hz
	B	2020–2045	H, He	13.6–14.1	4.7–4.3	0.5–1.5 Hz
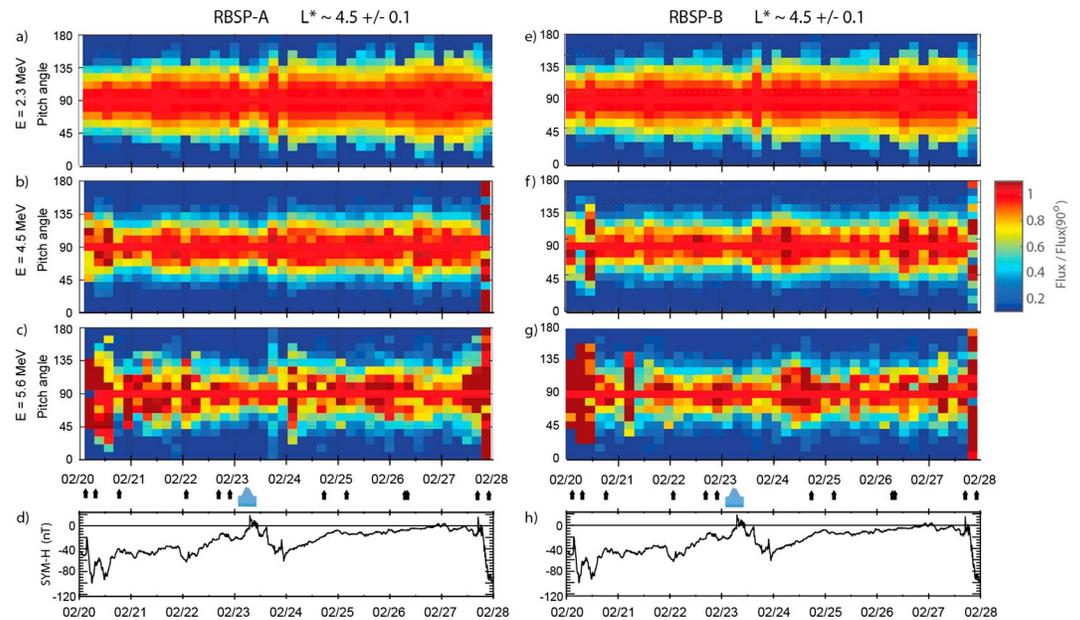
Figure 11. Pitch angle distributions of differential electron fluxes, normalized by the 90° pitch angle flux, at L* = 4.5 ± 0.1 in the 2.3, 4.5, and 5.6 MeV energy channels, respectively, observed by the REPT instrument on (a–c) RBSP-A and (e–g) RBSP-B from 20 to 28 February 2014. The fluxes are plotted on a linear scale according to the color bar at the right. Figures 11d and 11h and arrows above them repeat the *SYM-H* index and intervals of strong EMIC waves, as in Figure 10.

than those during this interval, so there is more scatter in the data, especially at the highest energy (5.6 MeV), because of lower particle counts.

The 23 February wave event (blue arrow) occurred simultaneous with a sharp temporary reduction in electron fluxes in all three energy ranges (Figure 10) and caused a narrowing of the normalized pitch angle distribution in each of the three ranges at both spacecraft during the subsequent pass (Figures 11a–11c and 11e–11g), but the narrowing was most pronounced at the higher energies (Figures 11b, 11c, 11f, and 11g). This narrower-angle range of trapped electron fluxes at higher energies is consistent with EMIC wave-induced losses observed by *Usanova et al.* [2014] and modeled by both *Usanova et al.* [2014] and *Kersten et al.* [2014]. The other EMIC wave events appeared to have no consistent temporal relation across energies to changes in either absolute flux (Figure 10) or normalized flux (Figure 11).

In order to focus more clearly on the effects of these EMIC waves on the fluxes of ultrarelativistic electrons fluxes, we show in Figure 12 the normalized pitch angle distribution of 5.6 MeV electrons from 0000 UT through 2400 UT 23 February 2014, as observed by both RBSP-A (a) and -B (c), shown whenever the respective spacecraft were at L shells above 3.0.

Immediately below each pitch angle spectrogram, in Figures 12b and 12d, are plots of the corresponding L and L* values traversed by RBSP-A and -B, respectively. The approximate L shells and times of most intense EMIC waves observed at Ministik Lake and at the Van Allen Probes are represented in both Figures 12b and 12d by orange and blue rectangles, respectively. Intense waves at Ministik Lake began near 0400 UT and ended near 0720 UT, and as noted above, their location was narrowly confined near L = 4.8. Although waves were observed by RBSP-A beginning near 0220 UT and by RBSP-B near 0340 UT, triggered EMIC emissions were observed only between 0705 and 0800 UT, in the L range between 5.7 and 4.7. The absence of wave activity after 0800 UT was temporal, because of the sudden drop in solar wind pressure, and thus not necessarily spatial. POES precipitating proton data shown in Figure 9 indicates that EMIC wave activity extended to L ~ 4, so it is possible that the L range of triggered emissions might have extended to this lower L value (as discussed in the following paragraphs). The region shaded more lightly in blue thus
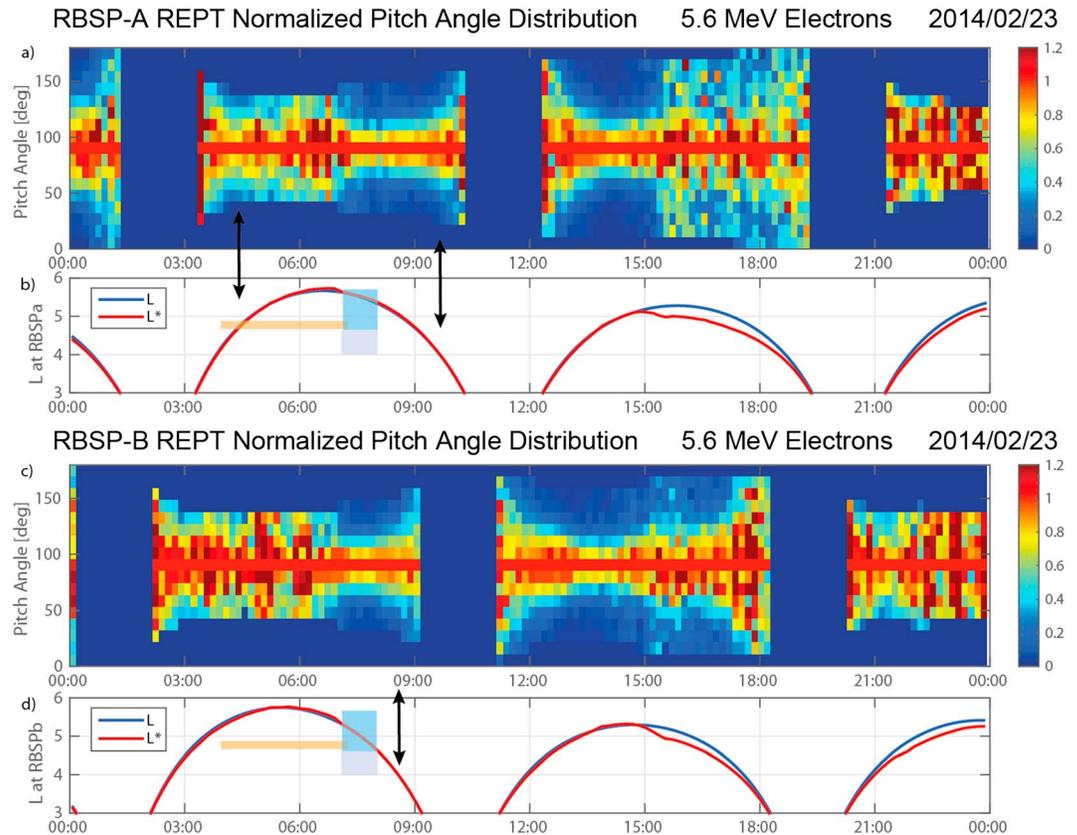
Figure 12. Normalized pitch angle distributions of 5.6 MeV electrons observed by the Van Allen Probes from 0000 UT through 2400 UT 23 February 2014. (a and c) The normalized fluxes, according to the color bar at the right, and (b and d) The L and L* values corresponding to the given times. The vertical arrows and shaded regions are described in the text.

extends from L = 4.7 down to L = 4.0, which was also the L value at which RBSP-B encountered the plasmapause near 0835 UT (RBSP-A encountered the PP near 1000 UT at L = 3.5).

The vertical black arrow connecting Figures 12a and 12b near 0425 UT indicates the time that RBSP-A crossed L = 4.8 on its outbound pass, some 30 min after the onset of EMIC activity at Ministik Lake (indicated by the left end of the orange shaded region). The normalized pitch angle distribution observed by RBSP-A (Figure 12a) at this time was sharply narrowed to near 90° for a short interval. In contrast, no similar narrowing was observed on RBSP-B (Figure 12c) during any of the outbound pass from 0230 to 0530 UT. This is consistent with the lack of overlap in Figure 12d between the L versus time trace and the orange shaded region, and the contrasting overlap between these two in Figure 12b.

The normalized pitch angle distributions at both RBSP-A and -B narrowed suddenly shortly after 0710 UT, corresponding to the time of onset of the triggered EMIC emissions (indicated by the left end of the blue shaded regions). This region, much wider in L than that observed near 0430 in RBSP-A near L = 4.8, extended down to approximately L = 4 at both spacecraft (vertical black arrows connecting Figures 12a and 12b near 0940 UT, and connecting Figures 12c and 12d near 0835 UT).

On the subsequent outbound pass of both RBSP-A and -B, the normalized pitch angle distributions became wider below L = 4.8, but remained very narrow at higher L values until ~1500 UT, at which time the main phase of a magnetic storm was under way (Figure 1). Pitch angle distributions at both RBSP-A and -B were again wider during the final inbound and outbound passes on this day. This indicates that either there were no additional EMIC waves during this storm main phase interval (consistent with their absence in available ground-based data) or if they occurred but were undetected, they were ineffective in causing a net depletion of ultrarelativistic electrons.

6. Discussion

The waves observed during this event are of interest in their own right for understanding the spatial extent of EMIC phenomena in Earth's magnetosphere when it is strongly compressed, and also because of their association with reductions in fluxes of ultrarelativistic electrons. The intensification of radiation belt fluxes during 22 and 23 February (during nonstorm conditions) shown in Figure 10 is of interest as well, and there is evidence that chorus plays a major role [*Liu et al.*, 2015; S. Wing, personal communication, 2014], but this intensification is beyond the scope of this study. In this section we review several features of EMIC waves that are relevant to this study, and the conditions under which EMIC waves are effective in depleting the radiation belts.

6.1. Location, Occurrence, and Properties of EMIC Waves

Much of the early theoretical and observational effort on EMIC waves was focused on regions near the plasmapause, and many recent studies have focused on their association with plasmaspheric plumes. However, several comprehensive satellite surveys have shown that waves occurred much more often at higher L shells than in the region of the plasmapause: *Anderson et al.* [1992a] and *Keika et al.* [2013], based on Active Magnetospheric Particle Tracer Explorers CCE data; *Fraser and Nguyen* [2001], based on CRRES data; and *Min et al.* [2012] and *Usanova et al.* [2012], based on THEMIS data. Statistically, these studies found only a minor enhancement in occurrence near the plasmapause. Theoretical support and statistical evidence for wave generation in plumes (regions of increased density outside the plasmapause) appears to be stronger [e.g., *Clausen et al.*, 2011], but a study by *Posch et al.*, 2010 comparing plume observations at geosynchronous orbit to EMIC observations from auroral ground stations, which because of horizontal ducting can sense waves originating over a wide L range, found only modest support for such an association.

Our current understanding is summarized well by *Keika et al.* [2013]: Two independent major processes cause EMIC wave excitation in the closed field line region of Earth's magnetosphere. The first externally triggers mostly H band waves on the dayside in the outer magnetosphere, because of solar wind compressions. The second internally excites mostly He band waves on the dusk-to-afternoonside in the inner magnetosphere during storm times, because of fresh injections of ions from the plasma sheet into the plasmapause and plume regions. In both processes some of the free energy in an anisotropic, more pancake-like velocity distribution of protons in the energy range from ~1 to ~200 keV is converted into wave energy, with the result that the pitch angle distribution tends to a more isotropic one, and a fraction of the energetic protons have their pitch angles moved into the loss cone, in which case the component of their motion parallel or antiparallel to the local magnetic field will cause them to reach the ionosphere and precipitate.

Keika et al. [2013] also noted that morning sector waves grow in resonance with lower energy ions than afternoon waves, consistent with lower energy plasma sheet ions convecting eastward from the tail, around the morningside. No plume is needed to trigger these waves. Such kilovolt-range protons are evident in both Figures 3 and 4 during the entire wave occurrence interval at both Van Allen Probes, and similar ~keV ion data were associated with EMIC waves in the outer dayside magnetosphere during compressions reported by *Engebretson et al.* [2002].

We have also noted in the introduction above that EMIC waves were observed throughout the morning sector, beginning shortly after midnight local time, and that this location is common during strong magnetospheric compressions. An additional event, on 17 January 2013, shows this same location: on this day both Van Allen Probes as well as near-conjugate ground-based observatories recorded intense EMIC waves shortly after midnight that were stimulated by a strong magnetospheric compression [*Weaver et al.*, 2013; M. R. Lessard, manuscript in preparation]. Although several major statistical studies [e.g., *Anderson et al.*, 1992a; *Fraser and Nguyen*, 2001] have indicated that the occurrence rate of EMIC waves in postmidnight local times are extremely low, a more detailed look at the observations of *Anderson et al.* [1992a] shows that at low L ($3 < L < 5$) the few events observed were relatively evenly distributed in local time. A similar pattern was found in the statistical study of CRRES data by *Halford et al.* [2010], who studied EMIC events before, during, and after magnetic storms: for $L > 5$ events most often occurred in the region from noon to dusk during the main and recovery phases of magnetic storms, but for $L < 5$ their Figure 4 indicates a much more uniform distribution in MLT during all three storm phases. We note also that the

CRRES mission did not complete one full precession in local time and thus did not collect much data in the dawn to noon sector.

The contrast between the radially narrow EMIC waves observed on this day in the dusk sector and the radially extended wave region in the dawn and noon sectors is striking, but several previous studies have also noted the wide variety of radial widths exhibited by EMIC waves on the dayside during large magnetospheric compressions. Low-altitude polar-orbiting satellite observations by Magsat [*Iyemori and Hayashi*, 1989], Viking [*Erlandson et al.*, 1990], and ST-5 [*Engebretson et al.*, 2008b] showed that regions of EMIC wave generation were often very narrow in L, down to ~ 0.1 L. However, *Engebretson et al.* [2002] reported both narrow and wide radial widths (up to and even exceeding 5 R_E), in observations from Polar, in a highly elliptical orbit in the outer dayside magnetosphere; the events with large radial width occurred during intervals of strong magnetospheric compressions.

The large radial width of the waves observed by the Van Allen Probes during this event and their location outside the plasmapause are also consistent with the observations by *Yahnin et al.* [2011] of proton aurorae with large latitudinal widths (up to ~10° MLAT) and their inference, based on an empirical model of plasmapause positions for 25 suboval proton aurora flashes, that at least the greater part of the proton aurora luminosity mapped outside the plasmasphere. A follow-up study by *Yahnina and Yahnin* [2014] of 582 proton precipitation events observed by NOAA satellites and triggered by magnetospheric compressions found that the majority of the events occurred at magnetic latitudes 5 to 10° higher than the latitudes that were either observed or inferred to be associated with cold-plasma boundaries.

The rising-tone hydrogen band-triggered emissions shown in RBSP-A data (Figure 5) and RBSP-B data (not shown) were first recognized in data from Cluster by *Pickett et al.* [2010] but have now also been identified in data from THEMIS [*Nakamura et al.*, 2014] and Polar [*Gamayunov et al.*, 2015] as well. The mechanism of their generation, similar to that of triggered VLF emissions, was first explained theoretically by *Omura et al.* [2010], and their effectiveness in depleting radiation belt electrons was discussed by *Omura and Zhao* [2012, 2013]. *Omura and Zhao* [2012, 2013] showed that EMIC rising-tone-triggered emissions in the hydrogen band (e.g., as shown in Figure 5) could trap resonant relativistic electrons, leading to rapid and efficient nonlinear pitch angle scattering without a strong dependence on ambient plasma density.

6.2. Conditions Under Which EMIC Waves are Effective in Depleting the Radiation Belts

Most theoretical studies have focused on the effectiveness of storm time dusk sector EMIC waves in high-density regions for pitch angle scattering relativistic electrons [e.g., *Summers and Thorne*, 2003; *Summers et al.*, 2007a, 2007b; *Jordanova et al.*, 2008; *Chen et al.*, 2011]. Although many of these studies have focused on helium band EMIC waves, which have been reported to dominate in the dusk sector in the statistical studies of EMIC waves noted above, some theoretical estimates indicated the effectiveness of hydrogen band EMIC waves as well [e.g., *Summers et al.*, 2007b; *Ukhorskiy et al.*, 2010]. These studies all assumed plasmaspheric or plume-like densities, however.

In addition to the observations reported here of EMIC waves and relativistic electron depletions in a region well outside the plasmapause, several recent observational studies have found EMIC wave-related scattering at other locations than dusk sector high-density regions, and at times not limited to storms. *Sandanger et al.* [2007] reported losses of relativistic electrons collocated with precipitating protons (interpreted as a consequence of the presence of EMIC waves) at all four of the local times they considered (0300, 0700, 1400, and 1700 MLT), and pointed out that precipitation of relativistic electrons due to weak pitch angle scattering by EMIC waves took place throughout the whole region where the pitch angle distribution of the protons is unstable to the growth of the ion cyclotron waves; that is, both inside and outside the plasmapause. *Sandanger et al.* [2009] reported large EMIC wave-induced losses of relativistic electrons during the recovery phase of geomagnetic storms (i.e., not during main phase). More recently, *Carson et al.* [2013] reported that the majority of the 2331 EMIC wave-driven relativistic electron precipitation (PPAREP) events they identified occurred outside the plasmasphere, at L values ~1 R_E greater than the plasmapause location determined from two different statistical models. They also found no clear relationship between the expected typical location of plasmaspheric plumes and the locations of the PPAREP events detected. It is clear that several observational studies, including this one, have reported relativistic electron scattering events in locations and physical regimes that are beyond the scope of most recent theoretical work.
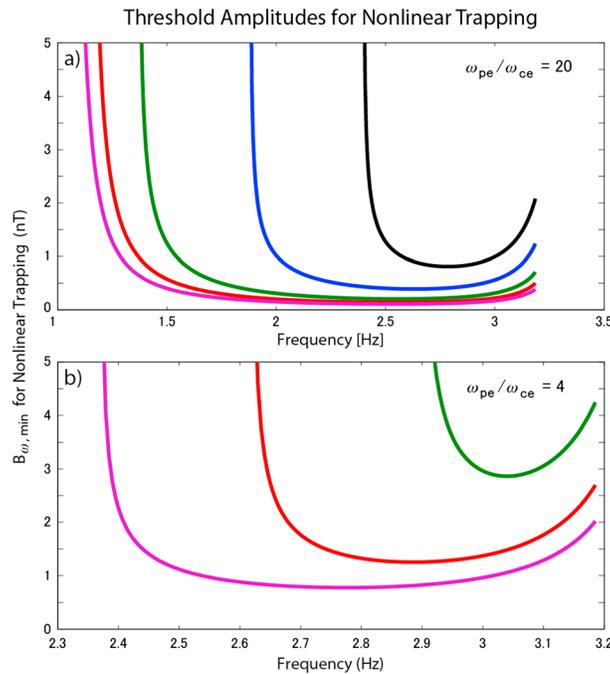
Figure 13. Threshold EMIC wave amplitudes for nonlinear trapping of relativistic electrons: (a) for $\omega_{pe}/\omega_{ce} = 20$, typical of higher-density plasmaspheric or plume conditions, and (b) for $\omega_{pe}/\omega_{ce} = 4$, consistent with the lower density location where waves were observed during this event. Energies of electrons are color coded as follows: black = 0.5 MeV, blue = 1 MeV, green = 2 MeV, red = 4 MeV, and magenta = 8 MeV.

As discussed by *Silin et al.* [2011], in a warm plasma the ability of EMIC waves to resonantly scatter MeV energy electrons is controlled by the value of the wave number. In contrast to conclusions drawn from cold-plasma theory, proximity of the wave emission to the local ion gyrofrequencies does not necessarily indicate strong coupling to the MeV electrons in warm plasmas. It is interesting to examine whether the EMIC waves observed on the Van Allen Probes on the dayside and on the ground at the Ministik Lake station in the premidnight sector might be related to the dynamics of the narrowing of the pitch angle distributions seen by REPT. Interestingly, the warm plasma analysis presented by *Silin et al.* [2011] can also be applied to the hydrogen band waves seen on the dayside by the Van Allen Probes. For example, cases 2, 4, and 6 in Table 1 of *Silin et al.* [2011] represent low-density warm plasma cases with increasing plasma beta at L = 7. For case 4 (their Figure 5d) there are two regions of growing EMIC waves: one close to and above the local helium gyrofrequency and another distinct emission close to one half of the hydrogen gyrofrequency. These two distinct growing EMIC waves have frequencies which bear remarkable similarity to the emissions observed by the Van Allen Probes in Figure 3 such as around 6 UT and later. For case 4 of *Silin et al.* [2011], the dispersion relation suggests both of these emissions could result in scattering of MeV electrons with minimum energies $> \sim 2$ MeV, consistent with the REPT observations presented here.

If the waves observed at Ministik Lake were generated in a region within the duskside plasmasphere, cold-plasma theory predicts that they would be quite effective in scattering radiation belt electrons. However, assuming that the Van Allen Probes on the dayside provide a good estimate of the location of the plasmapause in the premidnight sector during this nonstorm interval, then the waves observed at Ministik Lake and associated with the narrow regions of ion isotropy seen by NOAA 16 at L = 4.8 lie outside the plasmapause, in a region with number densities around 30–50 cm^{-3} (cf. Figure 3). Cases such as in Figure 5c in *Silin et al.* [2011] (case 3 from their Table 1) shows an example situation for warm plasma EMIC waves excited outside the plasmapause at L = 4. As shown in that figure, growing EMIC modes will be excited around and below the Helium gyrofrequency, which for sufficiently high plasma beta might resonate with ~ 1 MeV electrons. Future analysis offers the possibility of a more detailed comparison between the theoretical dispersion relation defined on the basis of the species-resolved HOPE warm ion data and the EMIC waves observed on the Van Allen Probes, including their effect on the MeV energy electrons.

We now return to the studies of *Omura and Zhao* [2012, 2013], which analyzed the effectiveness of triggered EMIC rising-tone emissions, which also occurred in the hydrogen band, for depleting radiation belt electrons. Figure 13 shows the energy thresholds, based on these studies and using a cold-plasma dispersion relation, for nonlinear trapping of resonant electrons with a range of energies, assuming a frequency sweep rate of the EMIC-triggered emissions of 1 Hz over 1 min, for (a) a high-density region (for $\omega_{pe}/\omega_{ce} = 20$) and (b) a low-density region (outside the plasmapause) corresponding to the 0700–0800 UT interval (for $\omega_{pe}/\omega_{ce} = 4$).

Densities assumed for protons, helium ions, and oxygen ions in producing this figure are 0.9, 0.05, and 0.05 of the electron density, respectively. The equatorial magnetic field magnitude selected for this calculation, 220 nT, was based on the following considerations: After the sudden pressure increase near 0705 UT and an initial rebound, the total field at the spacecraft location of RBSP-A (near −16° MLAT) increased gradually from 216 nT at 0710 UT to 220 nT at 0730 UT, and then increased somewhat more rapidly to 240 nT at 0800 UT. We have no direct knowledge of the magnetic field magnitude at the magnetic equator, but because the magnetic field near local noon beyond L ~ 5 is expected to be somewhat nondipolar (flattened near the equator) under these highly compressed conditions, we chose $B_{eq} = 220$ nT.

Figure 13a shows that hydrogen band EMIC-triggered emissions with amplitudes greater than 1 nT can precipitate all electrons > 0.5 MeV very efficiently in regions of high density. Outside the plasmasphere (Figure 13b), the parameter regime for which trapping and depletion can occur is considerably reduced, but it is still possible for highly relativistic electrons (>2 MeV) and for somewhat higher wave frequencies. The (energy-dependent) minimum amplitude for trapping also is larger for regions outside the plasmapause, but the wave amplitudes observed during this event considerably exceed the 1–3 nT thresholds shown in Figure 13b. The energy dependence shown in this figure is also consistent with the trend shown in Figure 11, in that the effectiveness of EMIC waves in depleting low pitch angle relativistic electrons is successively greater at 4.5 MeV and 5.6 MeV than at 2.3 MeV. This observed energy-dependent trend is also qualitatively consistent with Figure 3 of *Omura and Zhao* [2013] in showing that anomalous cyclotron resonance is satisfied for increasing pitch angles (toward 90°) as energy increases, although that figure was calculated assuming $\omega_{pe}/\omega_{ce} = 18$.

7. Summary and Conclusions

The EMIC wave event of 23 February 2014 is the longest-duration and most intense event we have yet observed with the Van Allen Probes. EMIC waves across a range of local times from midnight to nearly 18 MLT were stimulated by a gradual 4 h rise in solar wind pressure and subsequent sharp increases, while waves in the dusk-to-midnight sector appeared to be unrelated to compression effects.

The Van Allen Probes observed intense EMIC waves in the hydrogen band in the dawn and noon local time sectors, over a range of L shells outside the plasmapause, from ~4.5 to 6.4. NOAA POES and METOP data showed that the radial extent of 30–80 keV proton precipitation was broad, from 2 to at least 4 L shells wide, consistent with the L shells observed by the Van Allen Probes, and temporally varying. Our observation that the bandwidth of EMIC waves observed at Halley, Mondy, and Magadan was wider than that observed at RBSP also suggests the generation of EMIC waves across a range of L shells occurred across a broad range of local times. Only in the postdusk sector were waves observed with a narrow L range, and these were not temporally associated with the strongest compressions.

We have also pointed out that this event is only the most recent example of EMIC waves stimulated by large solar wind compressions that appeared over wide ranges of both local times and L shells. However, because this event was observed by a constellation of spacecraft and ground-based magnetometers, and because the Van Allen Probes spacecraft are well-instrumented to characterize the full range of highly energetic particles in the magnetosphere, it is possible to assess the effects that this wave event had on electrons in the outer radiation belt. Clear signatures of EMIC wave depletions of ultrarelativistic electrons were evident at both RBSP-A and -B, with timing consistent with a first dusk sector helium band wave event localized at L = 4.8 causing a depletion of relativistic electrons in a narrow L range (observed by only by RBSP-A) and a subsequent intense hydrogen band-triggered emission wave event causing depletions over a much wider range of L, consistent with the relatively wide range of L values of the observed EMIC waves observed by both Van Allen Probes. Also, as with other recent studies of the effects of EMIC waves on relativistic electrons, their effects on low pitch angle electrons were more pronounced as energies increased from 2.3 MeV to 5.6 MeV. Finally, although the effectiveness of EMIC waves in low-density regions in depleting relativistic electrons is not consistent with theoretical studies based on quasi-linear theory, we have demonstrated their consistency with the warm plasma theory presented by *Silin et al.* [2011] and with the nonlinear trapping mechanism presented by *Omura and Zhao* [2012, 2013].

The observations reported here suggest that studies of the effectiveness of EMIC waves for depleting the outer radiation belt should not focus exclusively on helium band EMIC waves, waves during storms, or those waves that occur in the afternoon local time sector in regions with greatly increased densities (in an extended plasmasphere or plume). Although the hydrogen band waves reported here are of very large amplitude, such amplitudes have been associated with other non-storm time solar wind compression events as well. It is hoped that these observations will stimulate renewed theoretical efforts to assess the effectiveness of compression-related, hydrogen band outer magnetospheric EMIC waves, as well as efforts to incorporate the warm plasma and nonlinear effects of EMIC wave generation and its impact on ultrarelativistic electrons in future simulations.

Appendix A

In this section we provide a detailed description of two of the Northern Hemisphere high-latitude dayside POES/METOP passes that detected precipitating ring current protons. Figures A1a, A1b, A2a, and A2b show electron observations, and Figures A1c, A1d, A2c, and A2d show proton observations. In Figures A1b, A1d, A2b, and A2d the dash-dotted lines designate trapped particles, and the solid lines precipitating particles.

Figure A1 shows a pass of the METOP 02 spacecraft, which between 0746 and 0756 UT passed equatorward ~ 1 h MLT west of the magnetic foot points of RBSP-A and -B. The auroral zones (characterized by isotropic particle fluxes), encountered in both the northbound and the southbound legs of this pass (~0740 to ~0743 and ~0747 to ~0748 UT) show equal fluxes of 30–80 keV protons along and normal to the magnetic field, whereas most of the intervals equatorward of this region show anisotropic distributions, with a very reduced flux along the magnetic field. However, three intervals of precipitating 30–80 keV proton fluxes are evident in the southbound leg between 0749:22 and 0752:50 (between 70° and 60° MLAT), all equatorward of the isotropic zone and also equatorward of the > 30 keV electron isotropic zone. No such intervals of precipitating 30–80 keV protons are seen equatorward of the >30 keV electron isotropic zone during the northbound leg (left-hand side of the figure). The gray shading in Figure A1 shows the approximate magnetic latitude of RBSP-A and -B, very near the most equatorward of the three intervals of precipitating protons observed by METOP 02.

Figure A2 shows an earlier pass of the NOAA 19 spacecraft, which passed very near the magnetic foot points of RBSP-A and -B at 0717 UT on its northbound leg, and observed precipitating 30–80 keV protons in one
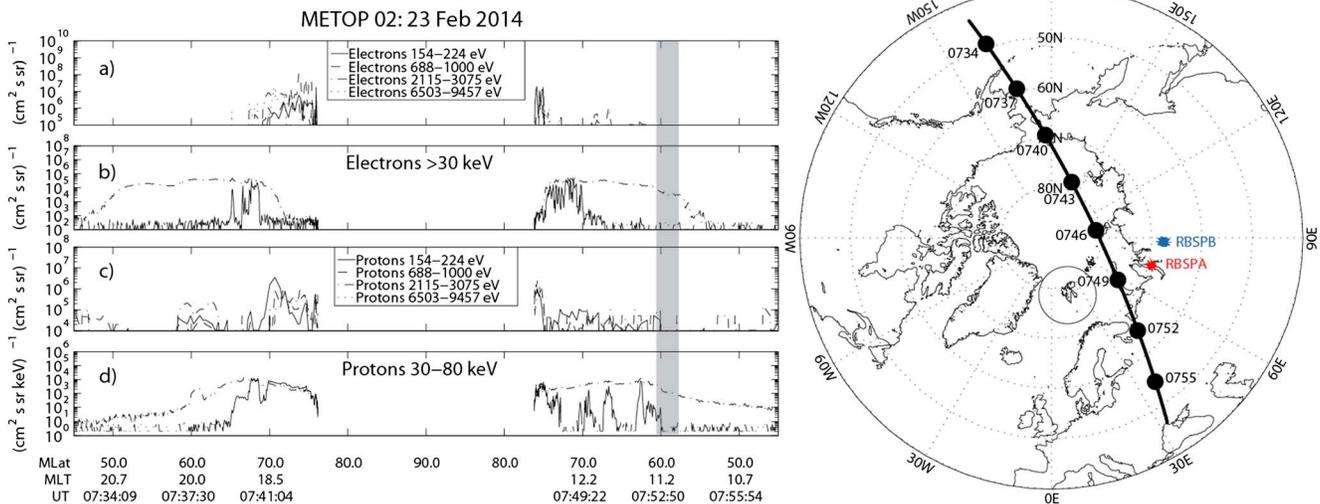
Figure A1. Energetic electron and proton data observed by METOP 02 between 0732 and 0757 UT 23 February 2014. (a and b) Electron observations and (c and d) proton observations. In Figures A1b and A1d the dash-dotted lines designate trapped particles and the solid lines precipitating particles. The gray shading shows the magnetic latitude of RBSP-A and -B.
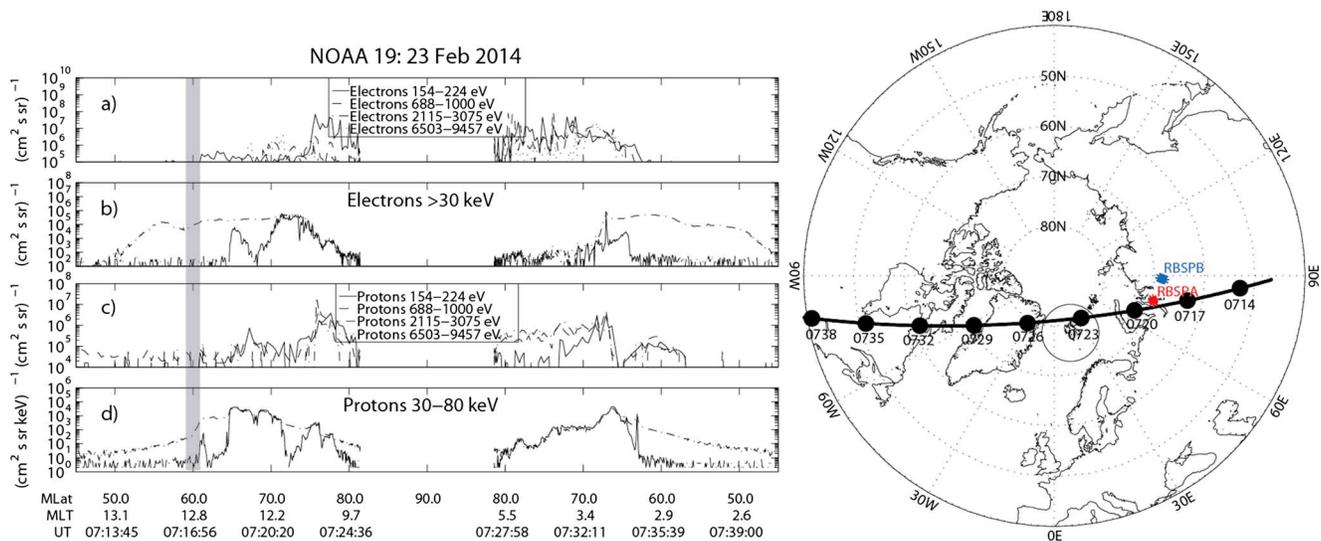
Figure A2. Energetic electron and proton data observed by NOAA 19 between 0712 and 0741 UT 23 February 2014, as in Figure A2. The gray shading shows the approximate MLAT of RBSP-A and -B.

narrow band at 61° MLAT, near the gray shaded area indicating the magnetic latitude of RBSP-A and -B, as well as a broad band from 64° to 72° MLAT (~0718 to ~0721 UT). Although this higher-latitude band overlaps somewhat with the equatorward edge of the isotropic electron zone, its presence is consistent with the third category of proton precipitation regions described by *Yahnina and Yahnin* [2014], which was observed near local noon during intervals of magnetospheric compression. Again, no such intervals of precipitating 30–80 keV protons were seen equatorward of the >30 keV electron isotropic zone during the other leg of this pass.

References

Anderson, B. J., and D. C. Hamilton (1993), Electromagnetic ion cyclotron waves stimulated by modest magnetospheric compressions, *J. Geophys. Res.*, 98, 11,369–11,382, doi:10.1029/93JA00605.

Anderson, B. J., R. E. Erlandson, and L. J. Zanetti (1992a), A statistical study of Pc 1–2 magnetic pulsations in the equatorial magnetosphere: 1. Equatorial occurrence distributions, *J. Geophys. Res.*, 97, 3075–3088, doi:10.1029/91JA02706.

Anderson, B. J., R. E. Erlandson, and L. J. Zanetti (1992b), A statistical study of Pc 1–2 magnetic pulsations in the equatorial magnetosphere: 2. Wave properties, *J. Geophys. Res.*, 97, 3089–3101, doi:10.1029/91JA02697.

Baker, D. N., et al. (2013), The Relativistic Electron-Proton Telescope (REPT) instrument on board the Radiation Belt Storm Probes (RBSP) spacecraft: Characterization of Earth's radiation belt high-energy particle populations, *Space Sci. Rev.*, 179, 337–381, doi:10.1007/s11214-012-9950-9.

Carson, B. R., C. J. Rodger, and M. A. Clilverd (2013), POES satellite observations of EMIC-wave driven relativistic electron precipitation during 1998–2010, *J. Geophys. Res. Space Physics*, 118, 232–243, doi:10.1029/2012JA017998.

Chen, L., R. M. Thorne, and J. Bortnik (2011), The controlling effect of ion temperature on EMIC wave excitation and scattering, *Geophys. Res. Lett.*, 38, L16109, doi:10.1029/2011GL048653.

Clausen, L. B. N., J. B. H. Baker, J. M. Ruohoniemi, and H. J. Singer (2011), EMIC waves observed at geosynchronous orbit during solar minimum, statistics and excitation, *J. Geophys. Res.*, 116, A10205, doi:10.1029/2011JA016823.

Cornwall, J. M. (1965), Cyclotron instabilities and electromagnetic emission in the ultra low frequency and very low frequency ranges, *J. Geophys. Res.*, 70, 61–69, doi:10.1029/JZ070i001p00061.

Denton, R. E., V. K. Jordanova, and B. J. Fraser (2014), Effect of spatial density variation and O+ concentration on the growth and evolution of electromagnetic ion cyclotron waves, *J. Geophys. Res. Space Physics*, 119, 8372–8395, doi:10.1002/2014JA020384.

Engebretson, M. J., W. K. Peterson, J. L. Posch, M. R. Klatt, B. J. Anderson, C. T. Russell, H. J. Singer, R. L. Arnoldy, and H. Fukunishi (2002), Observations of two types of Pc 1–2 pulsations in the outer dayside magnetosphere, *J. Geophys. Res.*, 107(A12), 1451, doi:10.1029/2001JA000198.

Engebretson, M. J., et al. (2008a), Pc1-Pc2 waves and energetic particle precipitation during and after magnetic storms: Superposed epoch analysis and case studies, *J. Geophys. Res.*, 113, A01211, doi:10.1029/2007JA012362.

Engebretson, M. J., J. L. Posch, A. M. Westerman, N. J. Otto, J. A. Slavin, G. Le, R. J. Strangeway, and M. R. Lessard (2008b), Temporal and spatial characteristics of Pc 1 waves observed by ST5, *J. Geophys. Res.*, 113, A07206, doi:10.1029/2008JA013145.

Erlandson, R. E., L. J. Zanetti, T. A. Potemra, L. P. Block, and G. Holmgren (1990), Viking magnetic and electric field observations of Pc 1 waves at high latitudes, *J. Geophys. Res.*, 95, 5941–5955, doi:10.1029/JA095iA05p05941.

Evans, D. E., and M. S. Greer (2000), Polar orbiting environmental satellite space environment monitor: 2. Instrument descriptions and archive data documentation, *Tech. Rep.*, Natl. Oceanic and Atmos. Admin., Boulder, Colo.

Francia, P., S. Lepidi, U. Villante, P. Di Giuseppe, and A. J. Lazarus (1999), Geomagnetic response at low latitude to continuous solar wind pressure variations during northward interplanetary magnetic field, *J. Geophys. Res.*, 104, 19,923–19,930, doi:10.1029/1999JA900229.

Fraser, B. J., and T. S. Nguyen (2001), Is the plasmapause a preferred source region of electromagnetic ion cyclotron waves in the magnetosphere?, *J. Atmos. Sol. Terr. Phys.*, *63*, 1225–1247.

Funsten, H. O., et al. (2013), Helium, Oxygen, Proton, and Electron (HOPE) mass spectrometer for the Radiation Belt Storm Probes mission, *Space Sci. Rev.*, *179*, 423–484, doi:10.1007/s11214-013-9968-7.

Fuselier, S. A., S. P. Gary, M. F. Thomsen, E. S. Claflin, B. Hubert, B. R. Sandel, and T. Immel (2004), Generation of transient dayside subauroral proton precipitation, *J. Geophys. Res.*, *109*, A12227, doi:10.1029/2004JA010393.

Gamayunov, K. V., M. J. Engebretson, M. Zhang, and H. K. Rassoul (2015), Source of seed fluctuations for electromagnetic ion cyclotron waves in Earth's magnetosphere, *Adv. Space Res.*, *55*, 2573–2583, doi:10.1016/j.asr.2015.02.024.

Grison, B., O. Santolik, N. Conrillleau-Wehrlin, A. Masson, M. J. Engebretson, J. S. Pickett, Y. Omura, P. Robert, and R. Nomura (2013), EMIC triggered chorus emissions in Cluster data, *J. Geophys. Res. Space Physics*, *118*, 1159–1169, doi:10.1002/jgra.50178.

Halford, A. J., B. J. Fraser, and S. K. Morley (2010), EMIC wave activity during geomagnetic storm and nonstorm periods: CRRES results, *J. Geophys. Res.*, *115*, A12248, doi:10.1029/2010JA015716.

Horne, R. B., and R. M. Thorne (1998), Potential waves for relativistic electron scattering and stochastic acceleration during magnetic storms, *Geophys. Res. Lett.*, *25*, 3011–3014, doi:10.1029/98GL01002.

Horne, R. B., M. M. Lam, and J. C. Green (2009), Energetic electron precipitation from the outer radiation belt during geomagnetic storms, *Geophys. Res. Lett.*, *36*, L19104, doi:10.1029/2009GL040236.

Iyemori, T., and K. Hayashi (1989), PC 1 micropulsations observed by Magsat in the ionospheric F region, *J. Geophys. Res.*, *94*, 93–100, doi:10.1029/JA094iA01p00093.

Jordanova, V. K., J. Albert, and Y. Miyoshi (2008), Relativistic electron precipitation by EMIC waves from self-consistent global simulations, *J. Geophys. Res.*, *113*, A00A10, doi:10.1029/2008JA013239.

Keika, K., K. Takahashi, A. Y. Ukhorskiy, and Y. Miyoshi (2013), Global characteristics of electromagnetic ion cyclotron waves: Occurrence rate and its storm dependence, *J. Geophys. Res. Space Physics*, *118*, 4135–4150, doi:10.1002/jgra.50385.

Kersten, T., R. B. Horne, S. A. Glauert, N. P. Meredith, B. J. Fraser, and R. S. Grew (2014), Electron losses from the radiation belts caused by EMIC waves, *J. Geophys. Res. Space Physics*, *119*, 8820–8837, doi:10.1002/2014JA020366.

Kletzing, C. A., et al. (2013), The Electric and Magnetic Field Instrument Suite and Integrated Science (EMFISIS) on RBSP, *Space Sci. Rev.*, *179*, 127–181, doi:10.1007/s11214-013-9993-6.

Lee, D.-Y., L. R. Lyons, and G. D. Reeves (2005), Comparison of geosynchronous energetic particle flux responses to solar wind dynamic pressure enhancements and substorms, *J. Geophys. Res.*, *110*, A09213, doi:10.1029/2005JA011091.

Lee, D.-Y., S. Ohtani, P. C. Brandt, and L. R. Lyons (2007), Energetic neutral atom response to solar wind dynamic pressure enhancements, *J. Geophys. Res.*, *112*, A09210, doi:10.1029/2007JA012399.

Liemohn, H. B. (1967), Cyclotron-resonance amplification of VLF and ULF whistlers, *J. Geophys. Res.*, *72*, 39–55, doi:10.1029/JZ072i001p00039.

Liu, S., et al. (2015), Van Allen Probes observations linking radiation belt electrons to chorus waves during 2014 multiple storms, *J. Geophys. Res. Space Physics*, *120*, 938–948, doi:10.1002/2014JA020781.

Lyons, L. R., and R. M. Thorne (1972), Parasitic pitch angle diffusion of radiation belt particles by ion cyclotron waves, *J. Geophys. Res.*, *77*, 5608–5616, doi:10.1029/JA077i028p05608.

Lyons, L. R., D.-Y. Lee, C.-P. Wang, and S. B. Mende (2005), Global auroral responses to abrupt solar wind changes: Dynamic pressure, substorm, and null events, *J. Geophys. Res.*, *110*, A08208, doi:10.1029/2005JA011089.

Mann, I. R., et al. (2008), The upgraded CARISMA magnetometer array in the THEMIS era, *Space Sci. Rev.*, *141*, 413–451, doi:10.1007/s11214-008-9457-6.

Mauk, B. H., et al. (2013), Science objectives and rationale for the Radiation Belt Storm Probes Mission, *Space Sci. Rev.*, *179*, 3–27, doi:10.1007/s11214-012-9908-y.

Meurant, M., J.-C. Gérard, B. Hubert, V. Coumans, C. Blockx, N. Østgaard, and S. B. Mende (2003), Dynamics of global scale electron and proton precipitation induced by a solar wind pressure pulse, *Geophys. Res. Lett.*, *30*(20), 2032, doi:10.1029/2003GL018017.

Millan, R. M., and R. M. Thorne (2007), Review of radiation belt relativistic electron losses, *J. Atmos. Sol. Terr. Phys.*, *69*, 362–377, doi:10.1016/j.jastp.2006.06.019.

Min, K., J. Lee, K. Keika, and W. Li (2012), Global distribution of EMIC waves derived from THEMIS observations, *J. Geophys. Res.*, *117*, A05219, doi:10.1029/2012JA017515.

Musko, S. B., C. R. Clauer, A. J. Ridley, and K. L. Arnett (2009), Autonomous low-power magnetic data collection platform to enable remote high latitude array deployment, *Rev. Sci. Instrum.*, *80*, 044501, doi:10.1063/1.3108527.

Nakamura, S., Y. Omura, S. Machida, M. Shoji, M. Nosé, and V. Angelopoulos (2014), Electromagnetic ion cyclotron rising tone emissions observed by THEMIS probes outside the plasmapause, *J. Geophys. Res. Space Physics*, *119*, 1874–1886, doi:10.1002/2013JA019146.

Olson, J. V., and L. C. Lee (1983), Pc1 wave generation by sudden impulses, *Planet. Space Sci.*, *31*, 295–302.

Olson, W. P., and K. A. Pfitzer (1982), A dynamic model of the magnetospheric magnetic and electric fields for July 29, 1977, *J. Geophys. Res.*, *87*, 5943–5948, doi:10.1029/JA087iA08p05943.

Omura, Y., and Q. Zhao (2012), Nonlinear pitch angle scattering of relativistic electrons by EMIC waves in the inner magnetosphere, *J. Geophys. Res.*, *117*, A08227, doi:10.1029/2012JA017943.

Omura, Y., and Q. Zhao (2013), Relativistic electron microbursts due to nonlinear pitch angle scattering by EMIC triggered emissions, *J. Geophys. Res. Space Physics*, *118*, 5008–5020, doi:10.1002/jgra.50477.

Omura, Y., J. Pickett, B. Grison, O. Santolík, I. Dandouras, M. Engebretson, P. M. E. Décréau, and A. Masson (2010), Theory and observation of electromagnetic ion cyclotron triggered emissions in the magnetosphere, *J. Geophys. Res.*, *115*, A07234, doi:10.1029/2010JA015300.

Pickett, J. S., et al. (2010), Cluster observations of EMIC triggered emissions in association with Pc1 waves near Earth's plasmapause, *Geophys. Res. Lett.*, *37*, L09104, doi:10.1029/010GL042648.

Posch, J. L., M. J. Engebretson, M. T. Murphy, M. H. Denton, M. R. Lessard, and R. B. Horne (2010), Probing the relationship between EMIC waves and plasmaspheric plumes near geosynchronous orbit, *J. Geophys. Res.*, *115*, A11205, doi:10.1029/2010JA015446.

Roederer, J. G. (1970), *Dynamics of Geomagnetically Trapped Radiation*, Springer, New York.

Sakaguchi, K., K. Shiokawa, A. Ieda, Y. Miyoshi, T. Otsuka, T. Ogawa, M. Connors, E. F. Donovan, and F. J. Rich (2007), Simultaneous ground and satellite observations of an isolated proton arc at subauroral latitudes, *J. Geophys. Res.*, *112*, A04202, doi:10.1029/2006JA012135.

Sandanger, M., F. Søraas, K. Aarsnes, K. Oksavik, and D. S. Evans (2007), Loss of relativistic electrons: Evidence for pitch angle scattering by electromagnetic ion cyclotron waves excited by unstable ring current protons, *J. Geophys. Res.*, *112*, A12213, doi:10.1029/2006JA012138.

Sandanger, M. I., F. Søraas, M. Sørbø, K. Aarsnes, K. Oksavik, and D. S. Evans (2009), Relativistic electron losses related to EMIC waves during CIR and CME storms, *J. Atmos. Sol. Terr. Phys.*, *71*, 1126–1144, doi:10.1016/j.jastp.2008.07.006.

Shiokawa, K., et al. (2010), The STEL induction magnetometer network for observation of high-frequency geomagnetic pulsations, *Earth Planets Space*, *62*, 517–524, doi:10.5047/eps.2010.05.003.

Shprits, Y. Y., D. Subbotin, A. Drozdov, M. E. Usanova, A. Kellerman, K. Orlova, D. N. Baker, D. L. Turner, and K.-C. Kim (2013), Unusual stable trapping of the ultrarelativistic electrons in the Van Allen radiation belts, *Nat. Phys.*, *9*(11), 699–703, doi:10.1038/nphys2760.

Silin, I., I. R. Mann, R. D. Sydora, D. Summers, and R. L. Mace (2011), Warm plasma effects on electromagnetic ion cyclotron wave MeV electron interactions in the magnetosphere, *J. Geophys. Res.*, *116*, A05215, doi:10.1029/2010JA016398.

Singer, H. J., L. Matheson, R. Grubb, A. Newman, and S. D. Bouwer (1996), Monitoring space weather with the GOES magnetometers, in *SPIE Conference Proceedings*, vol. 2812, edited by E. R. Washwell, pp. 299–308, GOES-8 and Beyond SPIE, Bellingham, Wash.

Søraas, F., K.,. M. Laundal, and M. Usanova (2013), Coincident particle and optical observations of nightside subauroral proton precipitation, *J. Geophys. Res. Space Physics*, *118*, 1112–1122, doi:10.1002/jgra.50172.

Spence, H. E., et al. (2013), Science goals and overview of the Radiation Belt Storm Probes (RBSP) Energetic Particle, Composition, and Thermal Plasma (ECT) suite on NASA's Van Allen Probes mission, *Space Sci. Rev.*, *179*, 311–336, doi:10.1007/s11214-013-0007-5.

Summers, D., and R. M. Thorne (2003), Relativistic electron pitch-angle scattering by electromagnetic ion cyclotron waves during geomagnetic storms, *J. Geophys. Res.*, *108*(A4), 1143, doi:10.1029/2002JA009489.

Summers, D., B. Ni, and N. P. Meredith (2007a), Timescales for radiation belt electron acceleration and loss due to resonant wave-particle interactions: 1. Theory, *J. Geophys. Res.*, *112*, A04206, doi:10.1029/2006JA011801.

Summers, D., B. Ni, and N. P. Meredith (2007b), Timescales for radiation belt electron acceleration and loss due to resonant wave-particle interactions: 2. Evaluation for VLF chorus, ELF hiss, and EMIC waves, *J. Geophys. Res.*, *112*, A04207, doi:10.1029/2006JA011993.

Takahashi, K., B. J. Anderson, and R. J. Strangeway (1990), AMPTE CCE observations of Pc 3–4 pulsations at L = 2–6, *J. Geophys. Res.*, *95*, 17,179–17,186, doi:10.1029/JA095iA10p17179.

Thorne, R. M., and C. F. Kennel (1971), Relativistic electron precipitation during magnetic storm main phase, *J. Geophys. Res.*, *76*, 4446–4453, doi:10.1029/JA076i019p04446.

Tsyganenko, N. A., and M. I. Sitnov (2005), Modeling the dynamics of the inner magnetosphere during strong geomagnetic storms, *J. Geophys. Res.*, *110*, A03208, doi:10.1029/2004JA010798.

Ukhorskiy, A. Y., Y. Y. Shprits, B. J. Anderson, K. Takahashi, and R. M. Thorne (2010), Rapid scattering of radiation belt electrons by storm time EMIC waves, *Geophys. Res. Lett.*, *37*, L09101, doi:10.1029/2010GL042906.

Usanova, M. E., et al. (2010), Conjugate ground and multisatellite observations of compression-related EMIC Pc1 waves and associated proton precipitation, *J. Geophys. Res.*, *115*, A07208, doi:10.1029/2009JA014935.

Usanova, M. E., I. R. Mann, J. Bortnik, L. Shao, and V. Angelopoulos (2012), THEMIS observations of electromagnetic ion cyclotron wave occurrence: Dependence on AE, SYMH, and solar wind dynamic pressure, *J. Geophys. Res.*, *117*, A10218, doi:10.1029/2012JA018049.

Usanova, M. E., et al. (2014), Effect of EMIC waves on relativistic and ultrarelativistic electron populations: Ground-based and Van Allen Probes observations, *Geophys. Res. Lett.*, *41*, 1375–1381, doi:10.1002/2013GL059024.

Weaver, C., M. R. Lessard, M. J. Engebretson, R. Millan, A. J. Halford, R. B. Horne, and H. J. Singer (2013), Ground and satellite EMIC waves observations in conjunction with BARREL electron precipitation, Abstract SM23C-07 presented at 2013 Fall Meeting, AGU, San Francisco, Calif., 10 Dec.

Wygant, J. R., et al. (2013), The electric field and waves instruments on the Radiation Belt Storm Probes mission, *Space Sci. Rev.*, *179*, 183–220, doi:10.1007/s11214-013-0013-7.

Yahnin, A., T. Yahnina, H. Frey, V. Pierrard, and T. Popova (2011), Location of the ion-cyclotron instability region relatively to plasmapause during magnetospheric compressions, in *Physics of Auroral Phenomena, Proc. XXXIV Annual Seminar, Apatity*, pp. 57–60, Kola Science Centre, Russian Academy of Science, Apatity, Murmansk Region, Russia.

Yahnin, A. G., T. A. Yahnina, H. U. Frey, T. Bösinger, and J. Manninen (2009), Proton aurora related to intervals of pulsations of diminishing periods, *J. Geophys. Res.*, *114*, A12215, doi:10.1029/2009JA014670.

Yahnina, T. A., and A. G. Yahnin (2014), Proton precipitation to the equator of the isotropic boundary during the geomagnetic storm on November 20–29, 2003, *Cosmic Res.*, *52*, 79–85.

Yahnina, T. A., H. U. Frey, T. Bösinger, and A. G. Yahnin (2008), Evidence for subauroral proton flashes on the dayside as the result of the ion cyclotron interaction, *J. Geophys. Res.*, *113*, A07209, doi:10.1029/2008JA013099.

Zhang, Y., L. Paxton, D. Morrison, B. Wolven, H. Kil, and S. Wing (2005), Nightside detached auroras due to precipitating protons/ions during intense magnetic storms, *J. Geophys. Res.*, *110*, A02206, doi:10.1029/2004JA010498.

Zhang, Y., L. J. Paxton, and Y. Zheng (2008), Interplanetary shock induced ring current auroras, *J. Geophys. Res.*, *113*, A01212, doi:10.1029/2007JA012554.